



# OPEN Tribological and corrosion behavior of $\text{Al}_2\text{O}_3$ interlayer reinforced friction stir welded AA6082-T6 joints

Abousoufiane Ouis<sup>1</sup>, Mohamed I. A. Habba<sup>2</sup>, Mohamed M. Z. Ahmed<sup>1✉</sup> & Waheed S. Barakat<sup>2</sup>

Friction stir welding (FSW) of thick extruded AA6082-T6 aluminum alloy plates presents challenges in maintaining optimal mechanical and corrosion properties. This study investigated the effects of incorporating  $\text{Al}_2\text{O}_3$  interlayer reinforcements on the microstructural, tribological, and corrosion behaviors of FSW joints. AA6082-T6 plates were friction stir welded with  $\text{Al}_2\text{O}_3$  interlayer strips at various levels of 0, 4, 8, and 12 vol%. The resulting joints were characterized using optical microscopy, electron microscopy, X-ray diffraction, hardness testing, potentiodynamic polarization, and pin-on-disk wear tests. The  $\text{Al}_2\text{O}_3$  reinforcement led to grain refinement, increased dislocation density, and enhanced microstrain in the weld zone. The relative density decreased with an increase in the  $\text{Al}_2\text{O}_3$  content. The Vickers hardness improved systematically across all thicknesses of the reinforced joints, with the highest values observed in the 12 vol%  $\text{Al}_2\text{O}_3$  specimen. The corrosion resistance of the reinforced joints improved significantly, approaching that of the base material. The wear resistance was enhanced in the reinforced joints with 8 vol%  $\text{Al}_2\text{O}_3$  specimen consistently showing the highest enhancement ratios under various load conditions. The incorporation of  $\text{Al}_2\text{O}_3$  interlayer reinforcements effectively mitigated the negative effects of FSW on AA6082-T6 joints, enhancing their microstructural, mechanical, tribological, and corrosion properties. Optimal performance was achieved with 8 vol%  $\text{Al}_2\text{O}_3$  reinforcement, balancing improvements in hardness, wear resistance, and corrosion behavior.

**Keywords** Friction stir welding, Tribology, Corrosion, AA6082, Alumina reinforcement, Metal matrix composites

AA6082-T6 is a heat-treatable aluminum (Al) alloy known for its high strength-to-weight ratio, good corrosion resistance, and excellent formability. It is widely used in the aerospace, automotive, and structural industries because of its favorable mechanical properties<sup>1–3</sup>. Due to its solid-state nature, friction stir welding (FSW) has emerged as a superior joining technique for Al alloys<sup>4–6</sup>. FSW is considered an energy-saving, environmentally friendly, and versatile technology, making it increasingly popular in high-demand fields such as aerospace and automotive industries. The solid-state nature of FSW minimizes the defects associated with fusion welding, such as porosity, hot cracking, and structural distortion. This results in improved joint quality, reduced post-weld processing, and enhanced mechanical properties of the welded structure<sup>4,7</sup>. Furthermore, FSW allows for joining dissimilar materials, which is particularly beneficial in industries seeking to optimize weight reduction and fuel efficiency<sup>8,9</sup>. FSW of thick Al plates, particularly AA6082-T6, presents several significant challenges that have been the focus of ongoing research in the field of materials joining<sup>10–12</sup>. One of the primary challenges in FSW of T6 Al plates is the significant microstructural changes that occur during the welding process. The T6 temper condition, achieved through solution heat treatment and artificial aging, results in a carefully controlled distribution of strengthening precipitates<sup>13,14</sup>. However, thermal cycling and severe plastic deformation during FSW can significantly alter the microstructure.

The heat generated during FSW can dissolve or coarsen the strengthening precipitates, particularly  $\text{Mg}_2\text{Si}$  in the AA6082-T6 alloy<sup>15–17</sup>. This results in weld zone (WZ) thermal softening and a significant reduction in the

<sup>1</sup>Mechanical Engineering Department, College of Engineering at Al-Kharj, Prince Sattam Bin Abdulaziz University, Al-Kharj 11942, Saudi Arabia. <sup>2</sup>Mechanical Department, Faculty of Technology and Education, Suez University, Suez 43221, Egypt. ✉email: moh.ahmed@psau.edu.sa

mechanical strength compared to the base material (BM). Hamada et al.<sup>18</sup> impacted thermal cycles during FSW on the AA6082-T6 alloy. They highlighted how the severe plastic deformation and high heat generated during FSW led to the dissolution or coarsening of strengthening precipitates, such as Mg<sub>2</sub>Si, in the WZ, contributing to thermal softening and reducing the mechanical properties compared to the initial material. In this context, Tamadon et al.<sup>19</sup> discussed how the elevated temperatures during FSW dissolve or coarsen Mg<sub>2</sub>Si precipitates, resulting in microstructural degradation and reduced mechanical properties, including hardness. They underscored the importance of controlling the thermal cycles to mitigate the reduction in the WZ properties. Adding reinforcements during FSW is an effective approach for enhancing the mechanical, tribological, and corrosion properties of friction stir welded (FSWed) joints. One widely used strategy involves particle reinforcement where micro- or nano-scale particles such as Al<sub>2</sub>O<sub>3</sub>, TiC, SiC, TiO<sub>2</sub>, or B<sub>4</sub>C are incorporated into the WZ<sup>20–24</sup>. These particles are typically pre-deposited along the welding path or introduced directly during the welding process. They enhance the properties of the joint through a dispersion-strengthening mechanism, acting as barriers to dislocation movement and increasing the hardness and tensile strength of the joint<sup>25–28</sup>. Furthermore, the wear resistance and high-temperature stability of these particles significantly improve their tribological performance<sup>28,29</sup>. Another effective strategy is interlayer reinforcement, where a metallic or composite strip is placed between the plates before welding<sup>30–32</sup>. This method ensures uniform distribution of the reinforcements and can provide multifunctional benefits, including enhanced mechanical strength and resistance to wear and corrosion<sup>33–35</sup>. In this context, Table 1 summarizes previous studies related to the FSW of Al alloys that applied the interlayer reinforcement strategy to improve the properties of welded joints.

Based on the literature review, a significant research gap exists in the application of ceramic-reinforced interlayer strips for the FSW of Al alloys. Much of the existing literature focuses on the use of metallic interlayer strips, such as Cu, Ni, and Al alloys, to improve the joint strength, ductility, and thermal stability. Ceramics, known for their superior thermal and wear resistance, can offer significant advantages in enhancing joint performance under extreme service conditions such as abrasive environments. Therefore, the current study focuses on investigating the role of Al/Al<sub>2</sub>O<sub>3</sub> interlayer strips in enhancing the microstructural, tribological, and corrosion behavior of the WZ structure of thick AA6082-T6 FSW joints. The introduction of these interlayer strips aims to address the inherent challenges associated with welding thick Al plates, such as microstructural heterogeneities, reduced wear resistance, and increased susceptibility to corrosion in the WZ. By incorporating Al/Al<sub>2</sub>O<sub>3</sub> interlayers during the FSW process, this study seeks to evaluate their effectiveness in improving the microstructure, hardness, and surface durability of joints under abrasive and corrosive conditions. This research focuses on exploring how these interlayer strips influence the properties of the developed WZ. This includes analyzing how the presence of Al<sub>2</sub>O<sub>3</sub> particles within the interlayer contributes to modifying the grain structure and wear resistance through dispersion strengthening and hardness improvement. This study also examined the ability of the interlayer to enhance corrosion resistance by mitigating galvanic differences and promoting a more uniform microstructure.

Materials and methods  
Joint and reinforcement materials

AA6082-T6 Al alloy plates (Egyptian Al Co., Aswan, Egypt) with dimensions of 200 mm in length, 100 mm in width, and 12 mm in thick were used in this study, as shown in Fig. 1a. The AA6082-T6 chemical composition primarily consisted of Al with 0.950% Si, 0.754% Mg, 0.664% Mn, and smaller amounts of Fe, Cu, Ti, Zn, and Cr. In terms of mechanical performance, AA6082-T6 exhibited an ultimate tensile strength of 332 MPa and an elongation of approximately 17%. Reinforcement was achieved using an Al<sub>2</sub>O<sub>3</sub> (Sigma Aldrich Company, Cairo, Egypt) interlayer in foil format, as shown in Fig. 2, incorporating ceramic particles with an average size of < 1 μm. Various volume fractions (0, 4, 8, and 12 vol%) of Al<sub>2</sub>O<sub>3</sub> were introduced using a novel interlayer strip technique to ensure homogeneous distribution throughout the stir zone (SZ) thickness. AA8011-O foil with a thickness of 11 μm was used to encapsulate the Al<sub>2</sub>O<sub>3</sub> powder and placed between the plates to reinforce the weld region. The AA8011-O chemical composition includes approximately 0.7 wt% Si, 0.5 wt% Fe and 0.5 wt% Si, and trace elements such as Mn, Mg, Zn, Ti, and Cu are also present in small amounts, less than 0.5 wt% each.

FSW process

The FSW of AA6082-T6 joints was performed using a conventional FSW tool fabricated from W302 cold-work steel and heat-treated to 52 HRC hardness. The tool features a tapered grooved pin and concentric circles on its concave shoulder, as shown in Fig. 1a. The FSW parameters were maintained constant at 600 rpm rotational speed, 100 mm/min welding speed, and a 2° tilt angle for all the welds. The FSW process was performed using the FSW machine model EG-FSW-M1, Suez University, Suez, Egypt<sup>38,39</sup>. Table 2 lists the 12 mm AA6082-T6 FSW joint and its corresponding reinforced joints with different Al<sub>2</sub>O<sub>3</sub> concentrations.

Refs.	Joint alloy	Joints	Type of reinforcement	Key results
36	AA6061-T6	Butt	Cu interlayer	Tensile strength of the Al/Cu/Al 285 MPa is higher than the Al/Al (218 MPa)
32	AA5052	Lap	Sn interlayer	The addition of the Sn interlayer further led to energy savings since the rotational speed required to achieve the higher tensile shear load
31	AA2024	Butt	AA7075 St interlayer rip	Applied a 1 mm-wide interlayer improved the tensile strength by 14.1% and the failure strain by 53% compared to the joint without interlayer
37	AA7075-T6, AA7475	Lap joint	SiC, Al <sub>2</sub> O <sub>3</sub> interlayers	SiC outperformed Al <sub>2</sub> O <sub>3</sub> in mechanical enhancements

Table 1. Summary of previous studies related to the interlayer strategy for FSW of al alloys.

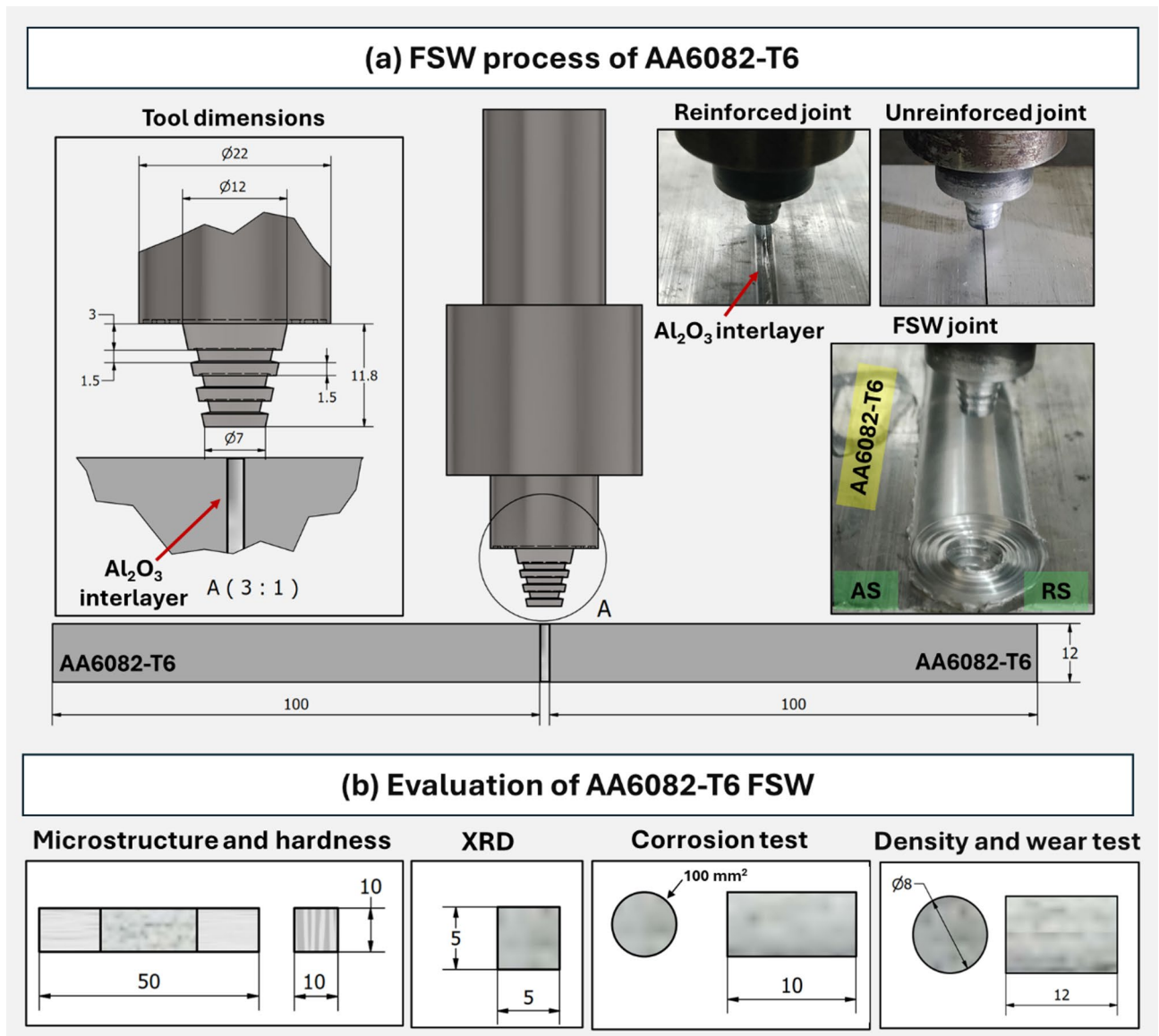


**Fig. 1.** Experimental work sketch of the FSW process for AA6082-T6 reinforced with  $\text{Al}_2\text{O}_3$  interlayer strips.

### Characterization methodology

The AA6082-T6 FSW joints were evaluated through microstructure and phase analyses using X-ray diffraction (XRD), densification properties, Vickers hardness, corrosion behavior, and wear performance (behavior and mechanisms). The characterization specimens were extracted from the FSWed joints, as illustrated in Fig. 3. Cross-sectional specimens were prepared perpendicular to the FSW direction for both macroscopic and microscopic examinations of the SZ. Figure 2b illustrates the main dimensions of the test samples extracted from the AA6082-T6 FSWed joints. The specimens underwent standard metallographic preparation, culminating in a  $0.05\text{ }\mu\text{m}$  surface finish. Metallographic analysis was performed using optical microscopy (Olympus BX-51 M) and field-emission scanning electron microscopy (FE-SEM) (QUANTA FEG 250, FEI Company, Hillsboro, USA) to examine the distinct microstructure features. Phase analysis of the SZ developed during the FSW process was conducted using X-ray diffraction (Bruker D8 Advance) with  $\text{Cu K}\alpha$  radiation ( $\lambda = 1.5406\text{ }\text{\AA}$ ). The diffractometer was operated at 40 kV and 30 mA, scanning across a  $2\theta$  range of  $20^\circ$ – $80^\circ$  with a step size of  $0.02^\circ$ . This analysis aimed to identify the phase transformations and potential intermetallic compound formation within the SZ (XRD test specimen dimensions; Fig. 1b). The densification properties in terms of relative density and relative porosity measurements of the WZ of the AA6082-T6 FSWed joints and their corresponding CWZ specimens CWZ/4, CWZ/8, and CWZ/12 were determined using the Archimedes principle method with distilled water as the liquid medium, following the JIS R2205-1992 standard. The mechanical property evaluation focused on the Vickers hardness of the FSWed joint WZ. Vickers hardness measurements of the SZ and adjacent regions were performed using a digital hardness tester (HWDV-75, TTS Unlimited, Osaka, Japan) under a 200 g load with a 10-second dwell time. The Vickers hardness was measured by collecting eight measurements for each developed

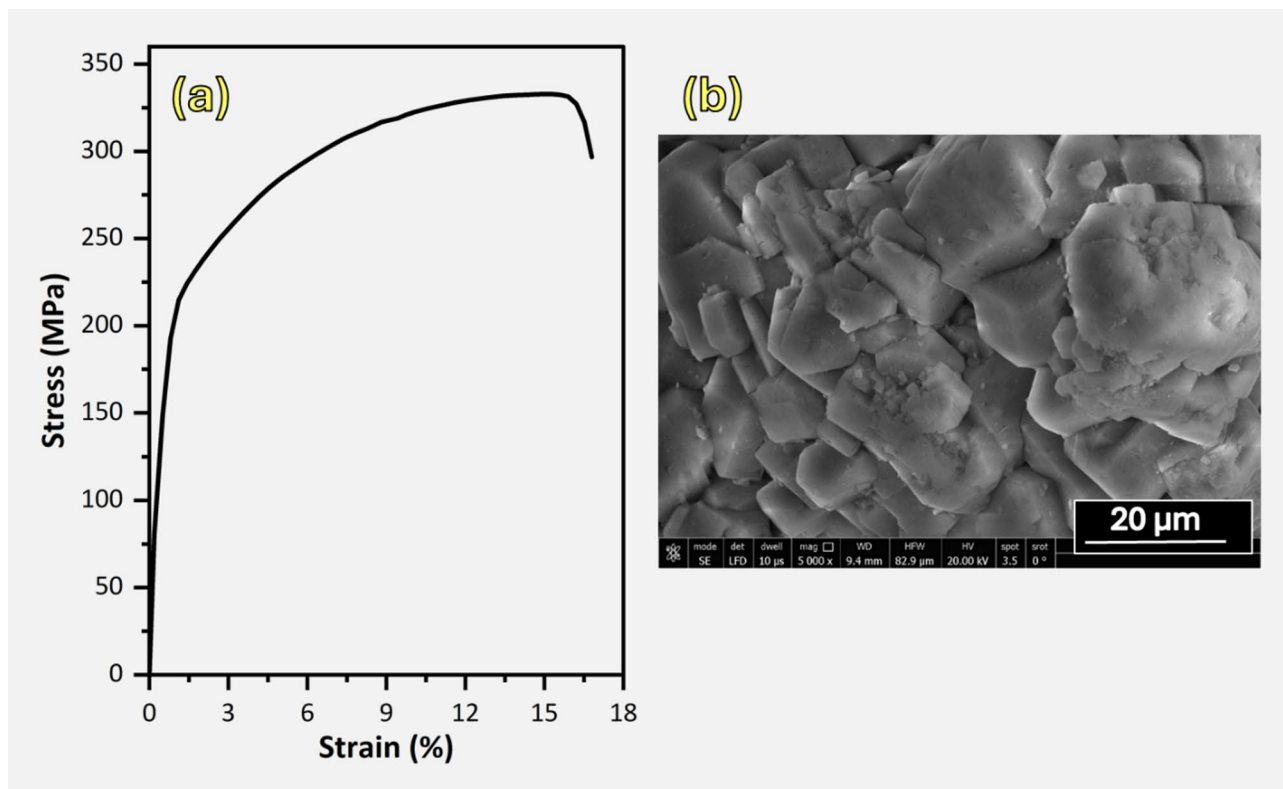


**Fig. 2.** (a) Stress–strain curve of AA6082-T6 BM and (b) SEM images of  $\text{Al}_2\text{O}_3$  ceramic particles.

No.	Joint code	Joint plate	$\text{Al}_2\text{O}_3$ concentration (vol%)
1	WZ/0	12 mm thickness AA6082-T6	0
2	CWZ/4		4
3	CWZ/8		8
4	CWZ/12		12

**Table 2.** Code of FSW AA6082-T6 joint and corresponding reinforced joints with different concentrations of  $\text{Al}_2\text{O}_3$ . WZ weld zone, CWZ composite weld zone.

zone across the welded joints. The interval distance between the middle layer and the upper and lower layers was 4 mm.

To investigate the corrosion characteristics of the AA6082-T6 BM and WZ of its FSWed joints, electrochemical testing was conducted according to ASTM G59-97 with a corrosion test specimen surface area of 100 mm<sup>2</sup> (Fig. 1b). The methodology involved stabilizing the open-circuit potential (OCP) by immersing the prepared specimens in a 3.5 wt% NaCl solution for 120 s. The specimens were meticulously prepared and mounted to ensure uniform exposure and accurate measurements. A three-electrode setup was employed, comprising a saturated calomel reference electrode, graphite counter electrode, and working electrode (AA6082-T6 and FSWed joints), which consisted of the working sample with a 1 cm<sup>2</sup> exposed surface. The potentiodynamic polarization technique was utilized to measure the corrosion behavior with a controlled potential sweep from −2 to +1 V relative to the reference electrode at a scan rate of 0.05 V/s. A potentiostat/galvanostat system supported by advanced electrochemical analysis software (Versa Studio Electrochemistry software package, version 2.60.4, Princeton Applied Research, Oak Ridge, TN, USA) was used to record the current-potential data. The corrosion rate (C.R.) was calculated using established equations, incorporating parameters such as  $i_{\text{corr}}$ , which is the corrosion current density (μA/cm<sup>2</sup>),  $W_p$ , the equivalent weight of the alloy,  $\rho$ , the density of the material (g/cm<sup>3</sup>), and A, the exposed surface area (cm<sup>2</sup>), as presented in Eq. 1:

$$CR = \frac{K \times i_{\text{corr}} \times W_E}{\rho \times A} \quad (1)$$

The wear behaviors of the AA6082-T6 BM and FSW joints, including those reinforced with  $\text{Al}_2\text{O}_3$  interlayers, were evaluated using a pin-on-disk wear test, adhering to the ASTM G99-04 standards. This method allows for



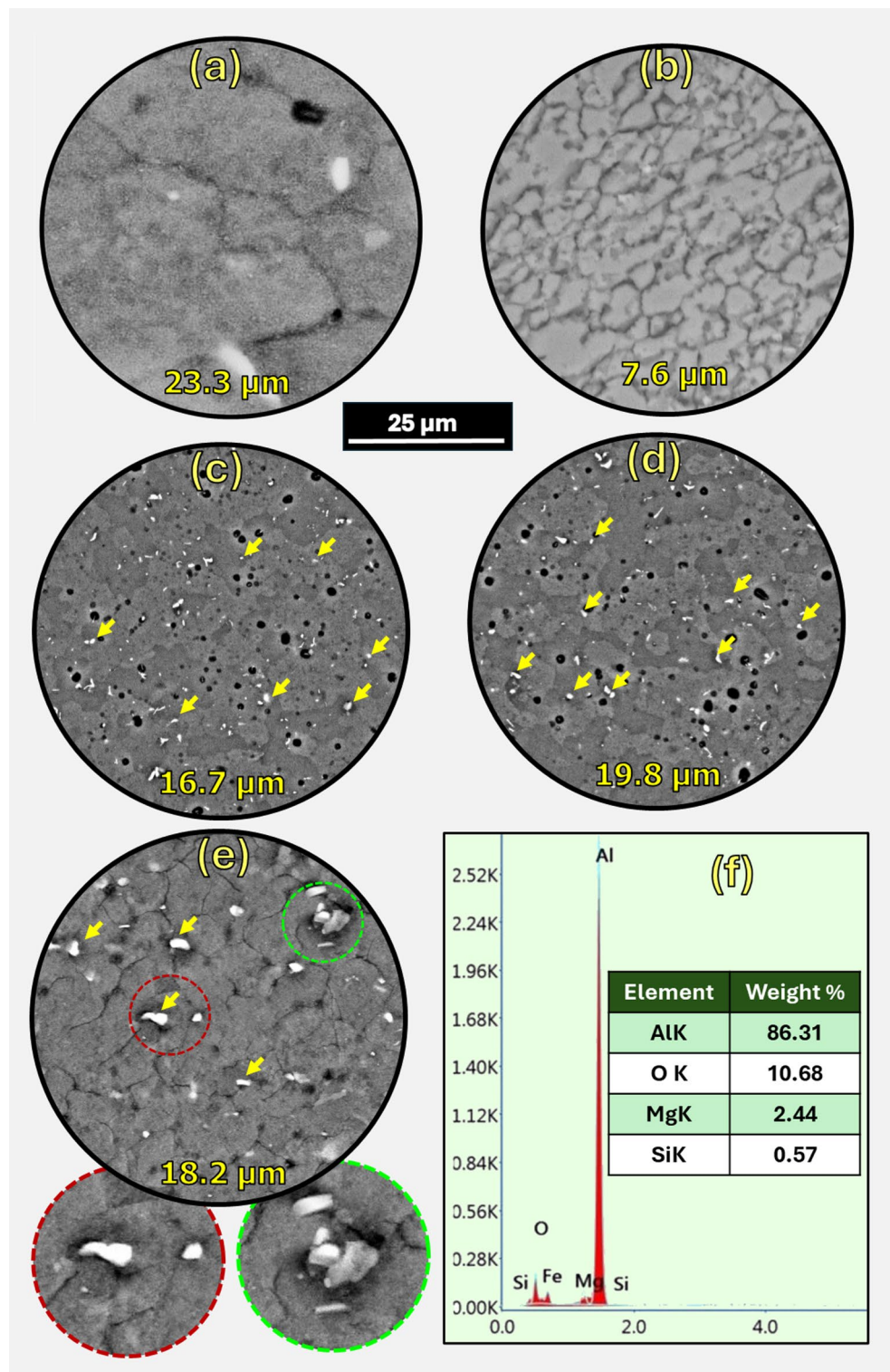


**Fig. 3.** Microstructure and grain size average of AA608-T6 BM and corresponding WZ of FSWed joints of (a) WZ/0, (b) CWZ/4, (c) CWZ/8, and (d) CWZ/12. (e) EDS of the CWZ of the CWZ/12 FSWed joint.

a controlled assessment of wear resistance under varying loads, sliding distances, and speeds. The cylindrical pin specimens extracted from the welded samples (including the CWZ reinforced with  $\text{Al}_2\text{O}_3$  interlayers) were machined to a uniform diameter of 8 mm and a height of 12 mm, as shown in Fig. 2b. The end surfaces were polished to a surface roughness of  $R_a = 0.2 \mu\text{m}$  to ensure consistent contact conditions during the testing. The steel disks, which served as counter materials, had a diameter of 50 mm and thickness of 10 mm. These disks were heat-treated to a hardness of  $60 \pm 2 \text{ HRC}$  and polished to a surface roughness of  $R_a = 0.1 \mu\text{m}$  to provide a

consistent counterface for all wear tests. Both the pins and disks were thoroughly cleaned with non-chlorinated solvents to remove contaminants and then dried to ensure accuracy in wear measurements. The wear tests were conducted under systematically varied conditions to evaluate the performance across a range of applied loads of 5, 10, 20, and 30 N and a sliding distance of 500 m. A consistent relative sliding velocity of 1.1 m/s was maintained throughout the test. Following the tests, the specimens were removed, cleaned to eliminate debris, and examined for the wear patterns. The wear behavior of each specimen was calculated using the wear volumetric loss rate ( $WV_l$ ) (Eq. 2) terms aligned with ASTM G99-04 guidelines. The weight loss of the wear-tested specimens was also recorded using a high-precision balance (0.0001 g electronic analytical balances, BA-E Series, Lixia District, Shandong, China), and the  $WV_l$  was derived using the material density by applying Archimedes principles. The wear mechanism of each tested specimen was detected through the worn surface of the wear-tested samples, which was evaluated using FE-SEM.

$$WV_l \text{ (mm}^3\text{/m)} = \frac{M \text{ (g)}}{\rho \text{ (g/cm}^3\text{)} \times S \text{ (m)}} \times 1000. \quad (2)$$

Where,  $WV_l$  : Wear volumetric loss rate,  $M$  : mass loss,  $\rho$  : density, and  $S$  : total sliding distance.

## Results and discussions

### Microstructure and phase analysis

Figure 3 illustrates the microstructural evolution in the (Fig. 3a) AA6082-T6 BM and various weld zones of the FSWed joints of (Fig. 3b) WZ/0, (Fig. 3c) CWZ/4, (Fig. 3d) CWZ/8, and (Fig. 3f) CWZ/12 regions. Furthermore, Fig. 3f shows the EDS of the CWZ/12 FSWed joint. It can be remarked that the microstructural evolution of AA6082-T6 BM and its corresponding weld zones of FSWed joints revealed distinct characteristics across different reinforcement levels. For the extruded AA6082-T6 BM, it can be revealed that the BM exhibited relatively large grains with an average size of around 23.3  $\mu\text{m}$  (Fig. 3a), which is characteristic of the T6 temper condition in extruded plates. Furthermore, bright regions corresponding to the  $\text{Mg}_2\text{Si}$  precipitates were distributed throughout the BM microstructure. Significant grain refinement occurred upon friction stir welding without reinforcement, resulting in an average grain size of approximately 7.6  $\mu\text{m}$ , as shown in Fig. 3b. This refinement is attributed to the severe plastic deformation and dynamic recrystallization processes inherent to FSW<sup>4,11,40</sup>. The fine equiaxed grains observed in the WZ/0 sample were a result of the breakdown of the original grain structure and subsequent recrystallization under the influence of frictional heat and mechanical stirring<sup>41–43</sup>. Incorporation of  $\text{Al}_2\text{O}_3$  reinforcement particles led to notable changes in the microstructural characteristics. The CWZ/4 joint, which contained 4 vol%  $\text{Al}_2\text{O}_3$  (Fig. 3c), displayed an intermediate grain size of 16.7  $\mu\text{m}$  with evidence of  $\text{Al}_2\text{O}_3$  particle distribution throughout the matrix. Similarly, the CWZ/8 joint (Fig. 3d) exhibited a grain size of 18.2  $\mu\text{m}$ , with  $\text{Al}_2\text{O}_3$  particles visible in the microstructure. The highest reinforcement level in CWZ/12 (Fig. 3e) resulted in a grain size of approximately 19.8  $\mu\text{m}$ , with distinctive features of  $\text{Al}_2\text{O}_3$  particle agglomeration sites. Black holes were observed in the microstructure at all reinforcement levels, which can be attributed to the pullout of  $\text{Al}_2\text{O}_3$  particles during the metallographic preparation. The microstructural evolution in the low level of grain coarsening of the CSZ of the FSWed joints exhibited a correlation between the presence of  $\text{Al}_2\text{O}_3$  particles and their thermal effects.  $\text{Al}_2\text{O}_3$  particles in the WZ significantly influenced the recrystallization mechanisms, serving as nucleation sites for new grains during dynamic recrystallization. This phenomenon arises from thermal expansion mismatches between  $\text{Al}_2\text{O}_3$  and the AA6082 matrix, generating stress-induced dislocations around the particles<sup>44,45</sup>. In contrast, the grain sizes in the  $\text{Al}_2\text{O}_3$ -reinforced joints increased compared to those in WZ/0. This unexpected growth may be attributed to  $\text{Al}_2\text{O}_3$  particles acting as localized heat reservoirs due to their lower thermal conductivity: around 237 W/m·K for  $\text{Al}$ <sup>46,47</sup> and around 30 W/m·K for  $\text{Al}_2\text{O}_3$ <sup>48,49</sup>. Such thermal behavior could potentially reduce the dynamic recrystallization (DRX) driving forces, thereby facilitating post-nucleation grain growth. It can be concluded that the microstructural evolution from the BM to various weld zones demonstrates the complex interplay between the thermomechanical effect of the FSW process and the presence of the  $\text{Al}_2\text{O}_3$  reinforcement. Although the initial FSW process led to significant grain refinement, the addition of  $\text{Al}_2\text{O}_3$  particles introduced competing grain pinning and localized heat generation mechanisms. The EDS analysis results presented in Fig. 3f confirm the presence of  $\text{Al}_2\text{O}_3$  particles within the composite weld zone. The elemental composition shown in Fig. 3f reveals a high Al content of 86.31% with significant O content of 10.68%, which corresponds to the  $\text{Al}_2\text{O}_3$  reinforcement particles, along with smaller amounts of 2.44% Mg and 0.57% Si. This elemental distribution confirms the successful incorporation of the  $\text{Al}_2\text{O}_3$  reinforcement into the WZ through the interlayer technique.

Figure 4 presents the colored elemental mapping of the composite CWZ/8 for the AA6082-T6 FSWed joint reinforced with 8 vol%  $\text{Al}_2\text{O}_3$ . The EDS maps revealed the spatial distributions of key elements, including Al, O, Mg, and Si. The Al map shows a uniform distribution throughout the matrix, as expected for the AA6082-T6. Notably, the oxygen map exhibited localized concentrations that correlated with the positions of the  $\text{Al}_2\text{O}_3$  particles, as shown in Fig. 4, confirming their presence and distribution within the WZ. The Mg and Si maps indicate a relatively homogeneous distribution of these alloying elements across the analyzed areas. This distribution suggests that the FSW process combined with  $\text{Al}_2\text{O}_3$  reinforcement did not lead to significant elemental segregation. The presence of Mg and Si is crucial for the formation of strengthening precipitates, such as  $\text{Mg}_2\text{Si}$ , which were observed in the BM microstructure (Fig. 3a) but appeared to be dissolved in the WZ owing to the thermal cycles during FSW. The high Al content of 88.99 wt% confirms the Al-rich matrix, while the oxygen content of 7.40 wt% corroborates the presence of  $\text{Al}_2\text{O}_3$  reinforcement particles. The Mg content was 2.82 wt% and Si content of 0.80 wt% levels (Fig. 4) are consistent with the nominal composition of the AA6082 alloy. EDS mapping and elemental analysis provided additional evidence for the effective incorporation of  $\text{Al}_2\text{O}_3$  nanoparticles within the CWZ, supporting the microstructural observations in Fig. 3.



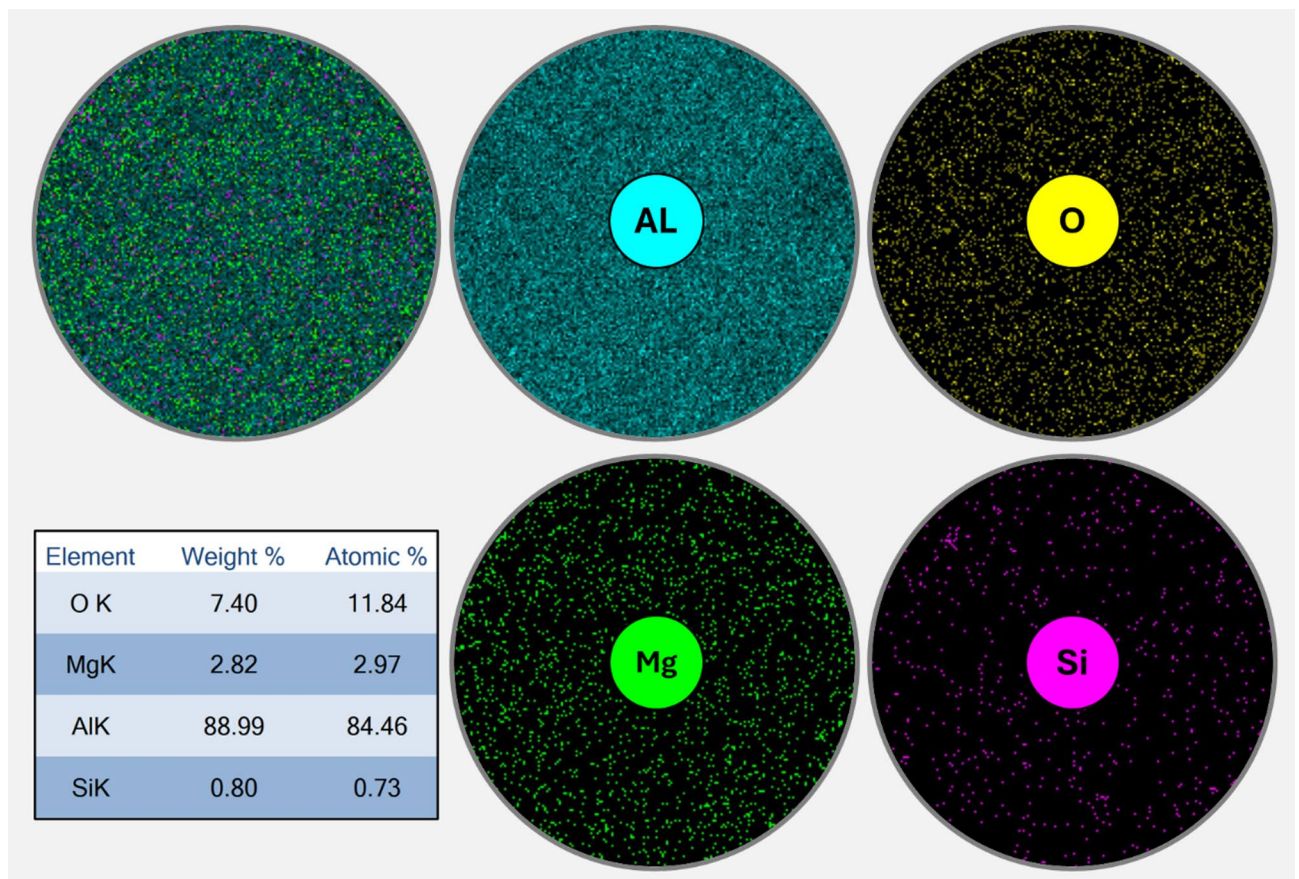


**Fig. 4.** Colored elemental mapping of the CWZ of AA6082-T6 FSWed joints reinforced with 8 vol%  $\text{Al}_2\text{O}_3$  (CWZ/8).

The XRD results in Fig. 5 demonstrate distinct phase compositions and structural transformations within the analyzed AA8011-O foil, AA6082-T6 BM, and FSWed joints WZs and their corresponding CWZ of the CWZ/8 and CWZ/12 specimens. The AA8011-O foil predominantly displayed characteristic Al peaks at  $2\theta$  values of  $38.5^\circ$ ,  $44.7^\circ$ ,  $65.1^\circ$ , and  $78.2^\circ$ , along with secondary  $\text{Al}_2\text{O}_3$  peaks at  $26.2^\circ$  and  $68.3^\circ$ . The presence of an oxide layer in the AA8011-O foil, as indicated by the distinct  $\text{Al}_2\text{O}_3$  peaks in the XRD results, was attributed to the natural passivation of Al. The oxide layer enhances the corrosion resistance by acting as a barrier to further oxidation and contributes to the compatibility of the AA8011-O foil as a reinforcement material in FSW by promoting the dispersion of the oxide particles within the WZ. The main peaks observed corresponded to Al for the AA6082-T6 BM. In addition, minor phases, including  $\text{Mg}_2\text{Si}$  ( $40.1^\circ$ ),  $\text{AlMnSi}$  ( $41.7^\circ$ ),  $\text{AlMn}$  ( $42.8^\circ$ ), and  $\text{Al}_2\text{Mn}$  ( $74.4^\circ$ ), were identified, indicating the influence of alloying elements on the microstructure and properties of the BM. The XRD patterns primarily showed Al peaks with no precipitates in the WZ of the unreinforced FSW joint (WZ/0). The absence of precipitates in the WZ of the unreinforced FSW joint results from thermal cycling and severe plastic deformation inherent to the FSW process<sup>50,51</sup>. During FSW, elevated temperatures and dynamic recrystallization can dissolve strengthening precipitates such as  $\text{Mg}_2\text{Si}$  in AA6082-T6<sup>52,53</sup>. However, incorporating  $\text{Al}_2\text{O}_3$  interlayers during FSW significantly altered the diffraction patterns of CWZ/8 and CWZ/12. The unclear presence of  $\text{Al}_2\text{O}_3$  phases in the CWZ/8 joint, as observed in the XRD patterns, can be attributed to the insufficient amount of oxide particles incorporated via the interlayer to form detectable phases in CWZ. At the same time, CWZ/12 revealed pronounced peaks for  $\text{Al}_2\text{O}_3$  at  $26.2^\circ$ ,  $35.2^\circ$ ,  $37.8^\circ$ ,  $43.4^\circ$ ,  $52.6^\circ$ ,  $57.5^\circ$ ,  $66.5^\circ$ , and  $68.3^\circ$ , indicating a higher degree of reinforcement integration. These results corroborate the efficacy of the interlayer approach in reinforcing the AA6082-T6 WZ to produce the AA6082-T6 CWZ structure, which is expected to have a significant impact on the physical, mechanical, tribological, and corrosion properties of AA6082-T6 FSWed joints.

The evaluation of the crystallite size, dislocation density, and dislocation increment across various regions of the AA6082-T6 BM and the corresponding WZ of the FSWed joints, including WZ/0, CWZ/4, CWZ/8, and CWZ/12, describes the effects of  $\text{Al}_2\text{O}_3$  reinforcement on the microstructural features. The crystallite size ( $D$ ) was evaluated using the Williamson-Hall equation (Eq. 3)<sup>54–56</sup>:

$$D = \frac{0.9\lambda}{\beta \cos \theta} \quad (3)$$

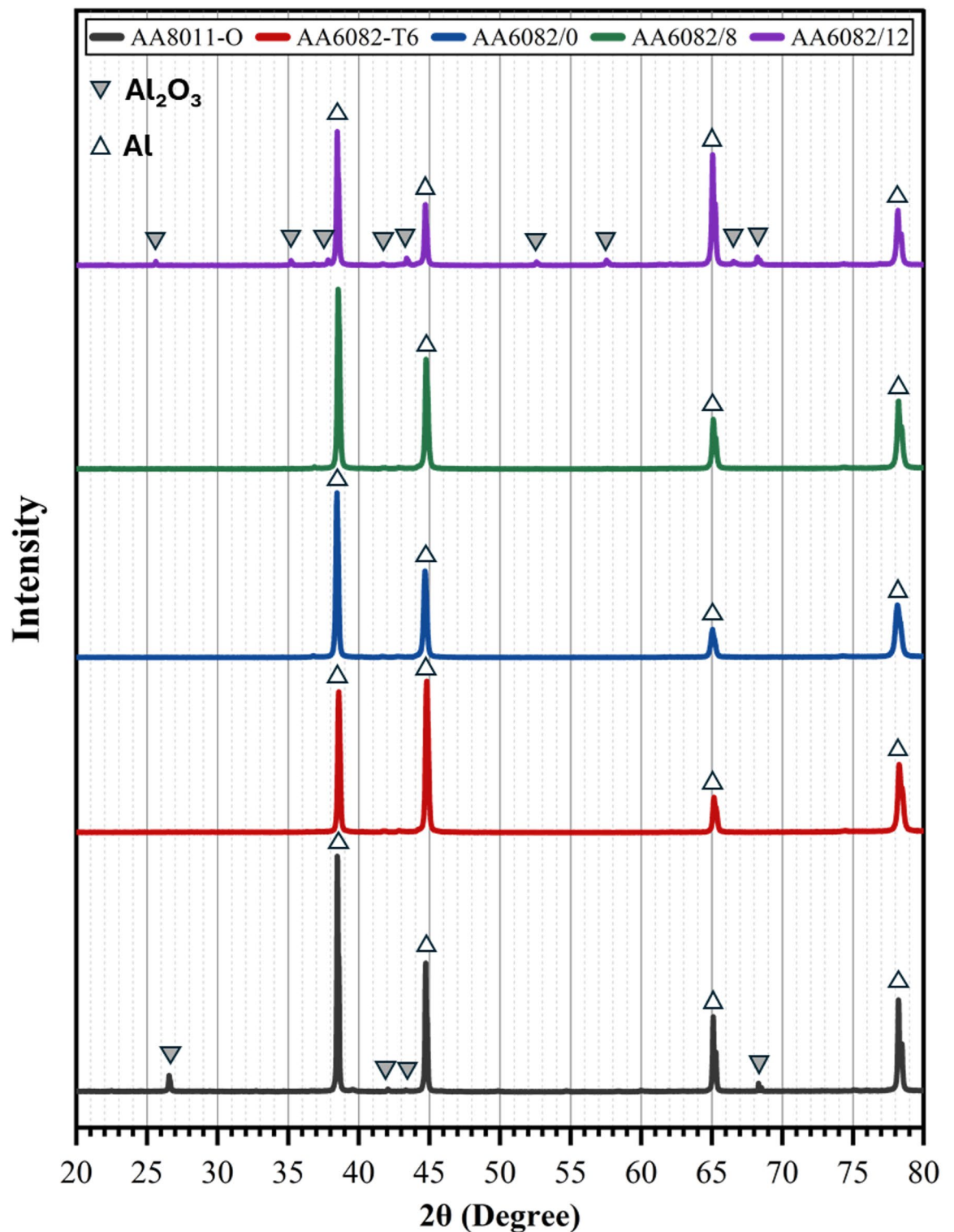


**Fig. 5.** XRD patterns of the AA8011-O Al foil, AA6082-T6 BM, and WZ of the FSWed joints of WZ/0, CWZ/8, and CWZ/12.

where  $\beta$  represents the peak width at half-maximum height (FWHM),  $\theta$  is the Bragg angle, and  $\lambda$  is the X-ray wavelength (0.1542 nm for Cu K $\alpha$  radiation). In addition, dislocation density ( $\rho_d$ ) related to the D can be calculated using Eq. 4<sup>54–56</sup>:

$$\rho_d = 1/D^2. \quad (4)$$



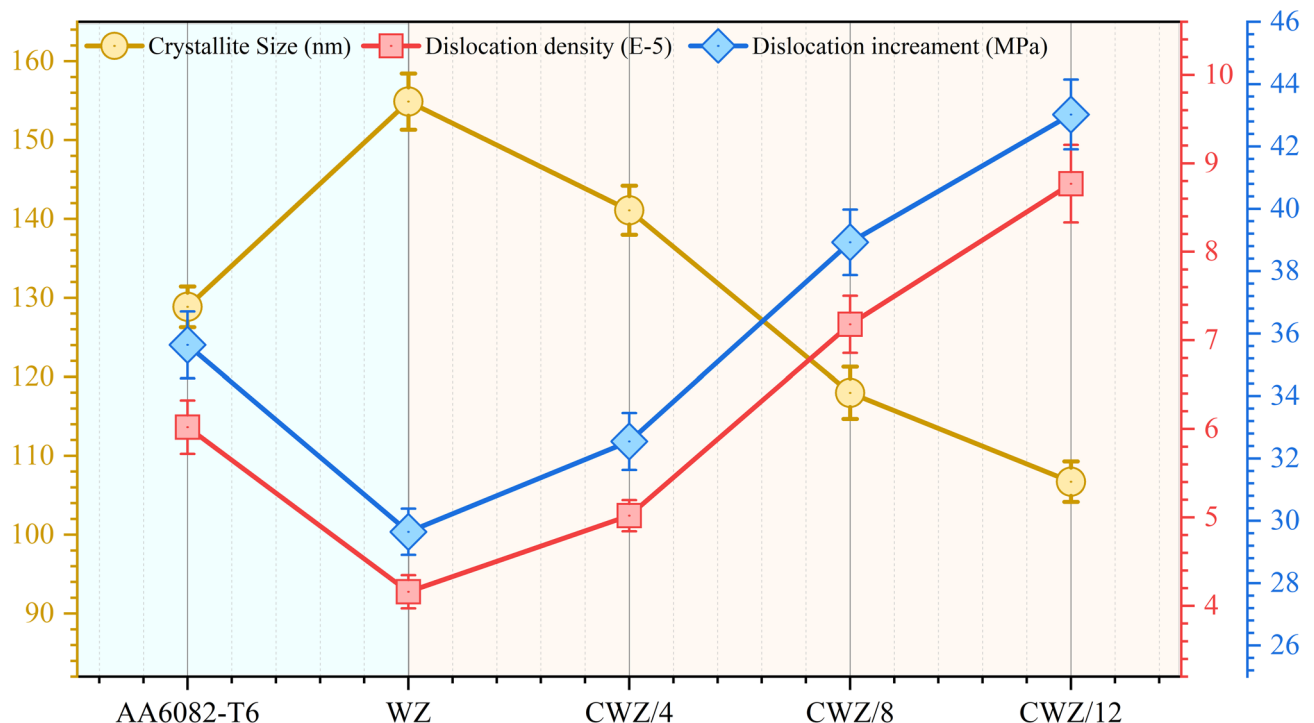
Furthermore, the increment in dislocation density can be calculated using Eq. 5<sup>56,57</sup>:

$$\Delta \sigma_{dis} = M \alpha G b \rho^{\frac{1}{2}}. \quad (5)$$

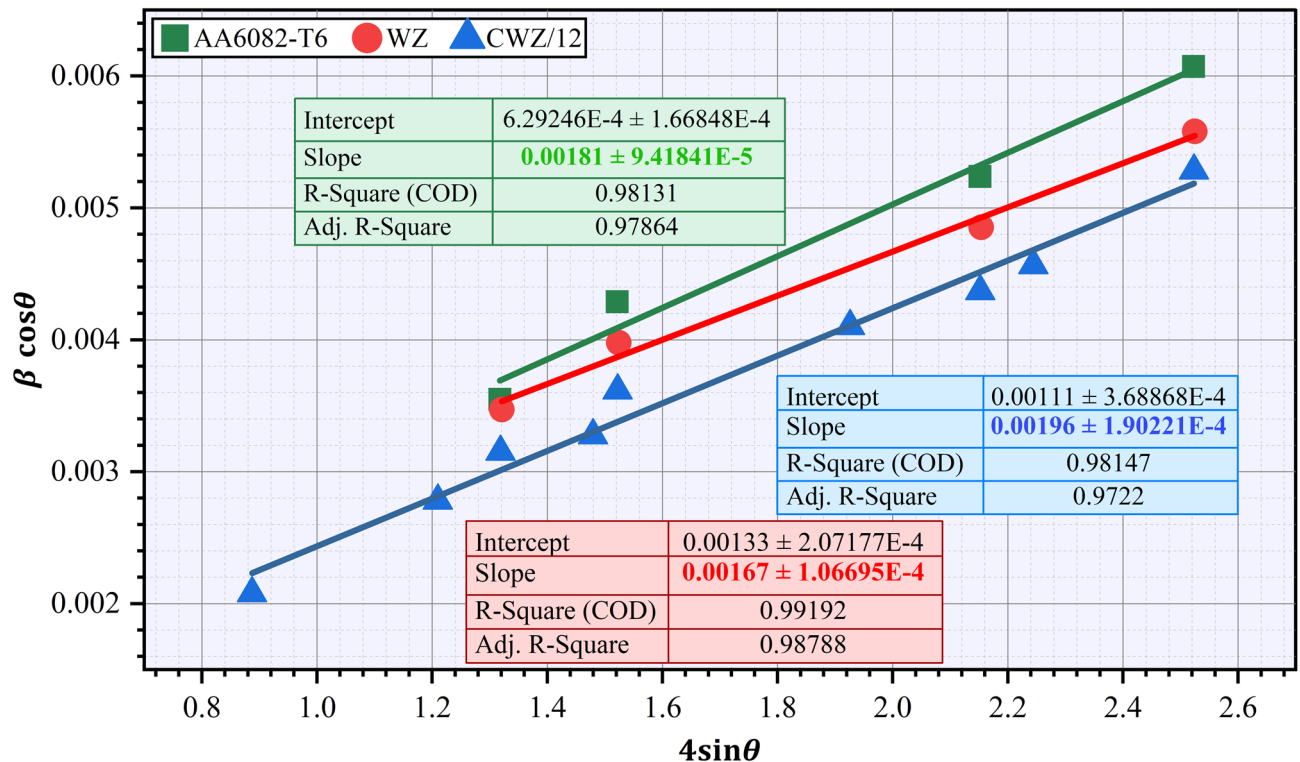
Where  $M$  is the Taylor factor,  $\alpha$  is the geometric factor of the Al alloy,  $G$  is the shear modulus,  $b$  is the Burgers vector, and  $\rho$  is the dislocation density.

Figure 6 shows the crystallite size in nm, dislocation density in  $\text{nm}^{-2}$ , and dislocation increment in MPa of the AA6082-T6 BM and the corresponding WZ of the FSWed joints of WZ/0, CWZ/4, CWZ/8, and CWZ/12. It can be remarked that the results of crystallite size, dislocation density, and dislocation increment revealed distinct trends across unreinforced and reinforced FSWed joints. As shown in Fig. 6, the crystallite size in the AA6082-T6 BM was 128.86 nm, indicating a relatively coarse grain structure attributed to the T6 temper condition. In the unreinforced WZ/0, the crystallite size increased to 154.89 nm. The inclusion of  $\text{Al}_2\text{O}_3$  interlayers in CWZ/4, CWZ/8, and CWZ/12 resulted in a progressive grain refinement. This trend was most pronounced in CWZ/12, where the crystallite size reduced to 106.73 nm, exhibiting a dispersion-strengthening effect of the ceramic particles. The observed grain refinement was consistent with the pinning effect of the  $\text{Al}_2\text{O}_3$  particles, which inhibited crystallite growth during recrystallization. For the dislocation density, the AA6082-T6 BM was recorded at  $6.02\text{E-}5 \text{ nm}^{-2}$ , and WZ/0, a decrease in dislocation density of  $4.16\text{E-}5 \text{ nm}^{-2}$  was noted. Furthermore, the dislocation increment exhibited a trend similar to that of dislocation density, as shown in Fig. 6. A baseline value of 35.64 MPa for the BM was observed, which decreased to 29.65 MPa for WZ/0. The AA6082-T6 BM exhibited a high dislocation density, corresponding to a high dislocation increment compared to the unreinforced WZ/0 joint, which was attributed to the initial extrusion and T6 heat treatment processes. Conversely, the addition of  $\text{Al}_2\text{O}_3$  to CWZ/4, CWZ/8, and CWZ/12 resulted in an increase in dislocation density, peaking at  $8.77\text{E-}5 \text{ nm}^{-2}$  for CWZ/12, as shown in Fig. 6. In addition, the dislocation increments in the reinforced zones exhibited increasing dislocation increments with increasing  $\text{Al}_2\text{O}_3$  levels in the WZ, with the highest value of 43.03 MPa recorded for CWZ/12. This trend highlights the role of  $\text{Al}_2\text{O}_3$  particles in creating dislocation networks owing to mismatched thermal and mechanical properties at the particle-matrix interface. In addition, the progressive increase aligns with the interaction between the dislocation motion and dispersed  $\text{Al}_2\text{O}_3$  particles, which act as barriers and promote the strain hardening.

After bringing  $\beta$  and  $\theta$  from the XRD pattern (Fig. 5) and by the linear fitting, as shown in Fig. 7, the microstrain ( $\epsilon$ ) is the slope of the fitting curve<sup>54,56</sup>. Microstrain analysis revealed distinct variations across the AA6082-T6 BM and corresponding WZ/0 and CWZ/12 joints. According to the Williamson-Hall plots presented in Fig. 7, the microstrain for the AA6082-T6 BM was determined to be  $0.00181 \pm 1.67\text{E-}4$ , whereas for the unreinforced WZ/0 joint, the value decreased to  $0.00167 \pm 1.07\text{E-}4$ . In contrast, the CWZ/12 joint exhibited an increased microstrain of  $0.00196 \pm 1.90\text{E-}4$ . This relatively high microstrain in the BM can be attributed to the residual strain induced during the extrusion process and T6 heat treatment of the base plate. In the unreinforced weld zone of the WZ/0 joint, the microstrain decreased to  $0.00167 \pm 1.07\text{E-}4$ , indicating the partial relief of



**Fig. 6.** Crystallite size, dislocation density, and dislocation increment of the AA6082-T6 BM and their corresponding WZ of the FSWed joints of WZ/0, CWZ/4, CWZ/8, and CWZ/12.



**Fig. 7.** Williamson–Hall plots of the AA6082-T6 BM and the corresponding WZ of the FSWed joints of WZ/0 and CWZ/12.

internal strains during the FSW process. However, the incorporation of  $\text{Al}_2\text{O}_3$  reinforcement in CWZ/12 led to a significant increase in the microstrain to  $0.00196 \pm 1.90\text{E-}4$ . This enhanced microstrain correlates with the reduced crystallite size of 106.73 nm and increased dislocation density of  $8.77\text{E-}5 \text{ nm}^{-2}$  observed in Fig. 7. The higher microstrain in CWZ/12 can be attributed to the presence of ceramic particles, which create localized strain fields at the particle-matrix interfaces owing to differences in the thermal and mechanical properties. The variation in the dislocation density and microstrain characteristics observed between the unreinforced and reinforced weld zones is anticipated to substantially influence the hardness, electrochemical, and tribological properties of the respective weld zones.

## Densification and hardness analysis

### Densification properties

The densification analysis revealed a clear correlation between the  $\text{Al}_2\text{O}_3$  content and the relative density/porosity characteristics of the WZ for both the unreinforced WZ/0 and  $\text{Al}_2\text{O}_3$ -reinforced joints. Figure 8 shows the densification properties of the WZ for the unreinforced joints of WZ/0 and  $\text{Al}_2\text{O}_3$ -reinforced joints CWZ/4, CWZ/8, and CWZ/12. It can be observed that the relative density of the WZ/0 joint was measured at  $99.21 \pm 0.5\%$ , with a corresponding relative porosity of  $0.79 \pm 0.40\%$ . This nearly full densification of the unreinforced joints can be attributed to the effective plastic deformation and material flow during the FSW process without any reinforcement particles interfering with consolidation<sup>21,58</sup>. However, as the  $\text{Al}_2\text{O}_3$  content increased, a notable decrease in the relative density was observed, accompanied by an increase in the porosity. For CWZ/4 (4 vol%  $\text{Al}_2\text{O}_3$ ), the relative density decreased to  $96.76 \pm 0.45\%$ , with porosity increasing to  $3.24 \pm 0.55\%$ . This trend continued with CWZ/8 (8 vol%  $\text{Al}_2\text{O}_3$ ), where relative density dropped further to  $95.26 \pm 0.40\%$ , and porosity rose to  $4.74 \pm 0.45\%$ , as shown in Fig. 8. The most significant reduction in densification was recorded for CWZ/12 (12 vol%  $\text{Al}_2\text{O}_3$ ), with a relative density of  $90.63 \pm 0.60\%$  and porosity of  $9.37 \pm 0.50\%$ , as shown in Fig. 8. The decrease in the relative density, combined with the increase in porosity with increasing  $\text{Al}_2\text{O}_3$  content, can be attributed to the presence of additional ceramic particles disrupting the plastic flow of the Al matrix and hampering the forging action under the tool shoulder. These ceramic particles reduce the ease of material consolidation within the CWZ. As the  $\text{Al}_2\text{O}_3$  content increased, the likelihood of void formation increased owing to the inadequate filling of small cavities and the lack of complete bridging between particles in the stirred region, ultimately translating into lower densification and higher porosity<sup>20–23</sup>. However, increasing the  $\text{Al}_2\text{O}_3$  particle content led to particle agglomeration. At higher concentrations, particularly in CWZ/12 with 12 vol%  $\text{Al}_2\text{O}_3$ , the  $\text{Al}_2\text{O}_3$  particles have a greater tendency to cluster together rather than distribute uniformly (Fig. 3e). These clusters create localized regions where complete material bonding is hindered, resulting in void formation and decreased density. Furthermore, the significant difference in the physical and mechanical properties between the  $\text{Al}_2\text{O}_3$  particles and Al matrix<sup>49,59</sup> contributes to the interface-related porosity<sup>49,59</sup>. The ceramic particles, which are much harder and more resistant to deformation than the AA6082 matrix, create stress concentrations at the

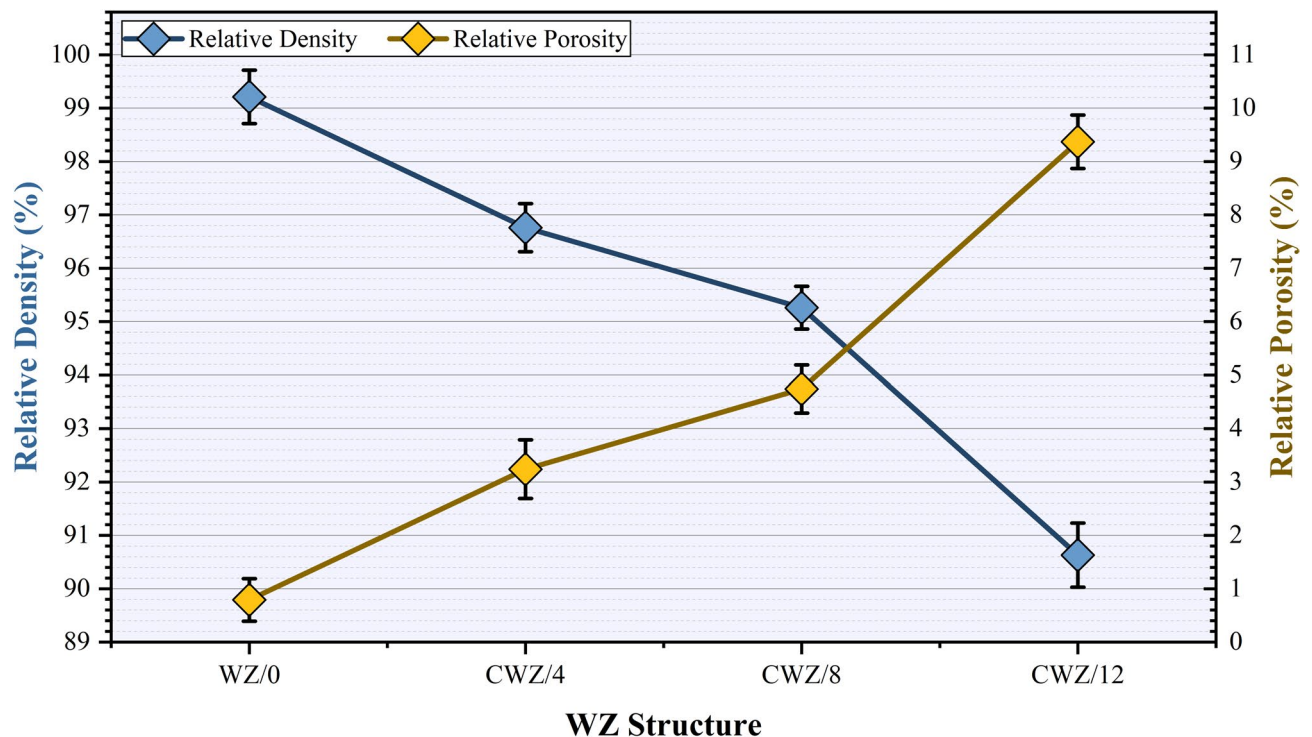


**Fig. 8.** Densification properties (relative density and relative porosity) of WZ for WZ/0, CWZ/4, CWZ/8, and CWZ/12 FSWed joints.

particle-matrix interfaces during the welding process. These stress discontinuities can lead to the formation of microvoids, particularly evident in the substantial decrease in the relative density to 90.63% for the CWZ/12. The progressive nature of this density reduction from 99.21% for WZ/0 to 96.76% for CWZ/4, 95.26% for CWZ/8, and 90.63% for CWZ/12, as shown in Fig. 8, demonstrates that the effect became more pronounced as the ceramic particle content increased. This trend aligns with the established principles of powder metallurgy and composite material processing<sup>59–62</sup>. It can be concluded that the incorporation of  $\text{Al}_2\text{O}_3$  in CWZ/4, CWZ/8, and CWZ/12 reduced the relative density by 2.47%, 3.98%, and 8.65%, respectively, compared to the WZ of the unreinforced joint, as shown in Fig. 8.

#### Hardness properties

The Vickers hardness distributions across different layers of the FSWed zones were systematically evaluated to assess the influence of the  $\text{Al}_2\text{O}_3$  reinforcement content on the joints' mechanical properties. Vickers hardness measurements were conducted across three distinct layers (upper, middle, and lower) of the WZ for the unreinforced joints and the CWZ for the reinforced joints CWZ/4, CWZ/8, and CWZ/12, as depicted in Fig. 9. It can be remarked that the unreinforced joint (WZ/0) exhibited a characteristic hardness gradient across its thickness, with values ranging from 91.1 HV in the upper layer to 109.5 HV in the lower layer compared to 117.5 HV for the AA6082-T6 BM. These results highlight the intrinsic characteristics of the WZ after FSW, on the first hand, where thermal softening effects dominate owing to the dissolution of strengthening precipitates, such as  $\text{Mg}_2\text{Si}$ . This trend is consistent with previous studies that observed reduced hardness in the WZ of AA6082-T6 joints caused by thermal cycling and dynamic recrystallization during FSW<sup>11,63</sup>. However, the vertical hardness variation WZ of WZ/0 can be attributed to the inherent thermal gradient and varying degrees of plastic deformation experienced during FSW. The lower layer demonstrated superior hardness owing to more effective material consolidation and reduced thermal exposure compared to the upper layer, which experienced direct contact with the tool shoulder<sup>64,65</sup>. The incorporation of  $\text{Al}_2\text{O}_3$  particles led to a systematic enhancement in the hardness across all layers. The CWZ/4 specimen, containing 4 vol%  $\text{Al}_2\text{O}_3$ , showed improved hardness values of 126.6 HV, 107.6 HV, and 117.7 HV in the upper, middle, and lower layers, respectively. This trend continued with increasing reinforcement content, reaching higher values in the CWZ/12 specimen, which was reinforced with 12 vol%  $\text{Al}_2\text{O}_3$ , which exhibited hardness measurements of 128.3 HV, 130.5 HV, and 132.6 HV across the three layers. It can be observed that the dominant mechanism controlling the hardness in the CWZ of the reinforced joints is the presence and distribution of  $\text{Al}_2\text{O}_3$  particles, rather than precipitates or grain refinement effects. This is evidenced by the substantial increase in hardness with increasing  $\text{Al}_2\text{O}_3$  content, which is related to the increase in dislocation density, as shown in Fig. 6. This trend was corroborated by the XRD analysis results, which provided an understanding of the microstructural changes that occurred at the atomic level. The dispersion strengthening effect was evident from the increasing dislocation density values observed in the XRD analyses. For the unreinforced WZ/0 joint, the dislocation density was measured at  $4.16\text{E}-5 \text{ nm}^{-2}$ , which increased progressively with the  $\text{Al}_2\text{O}_3$  content, reaching  $8.77\text{E}-5 \text{ nm}^{-2}$  for the CWZ/12 joint, as



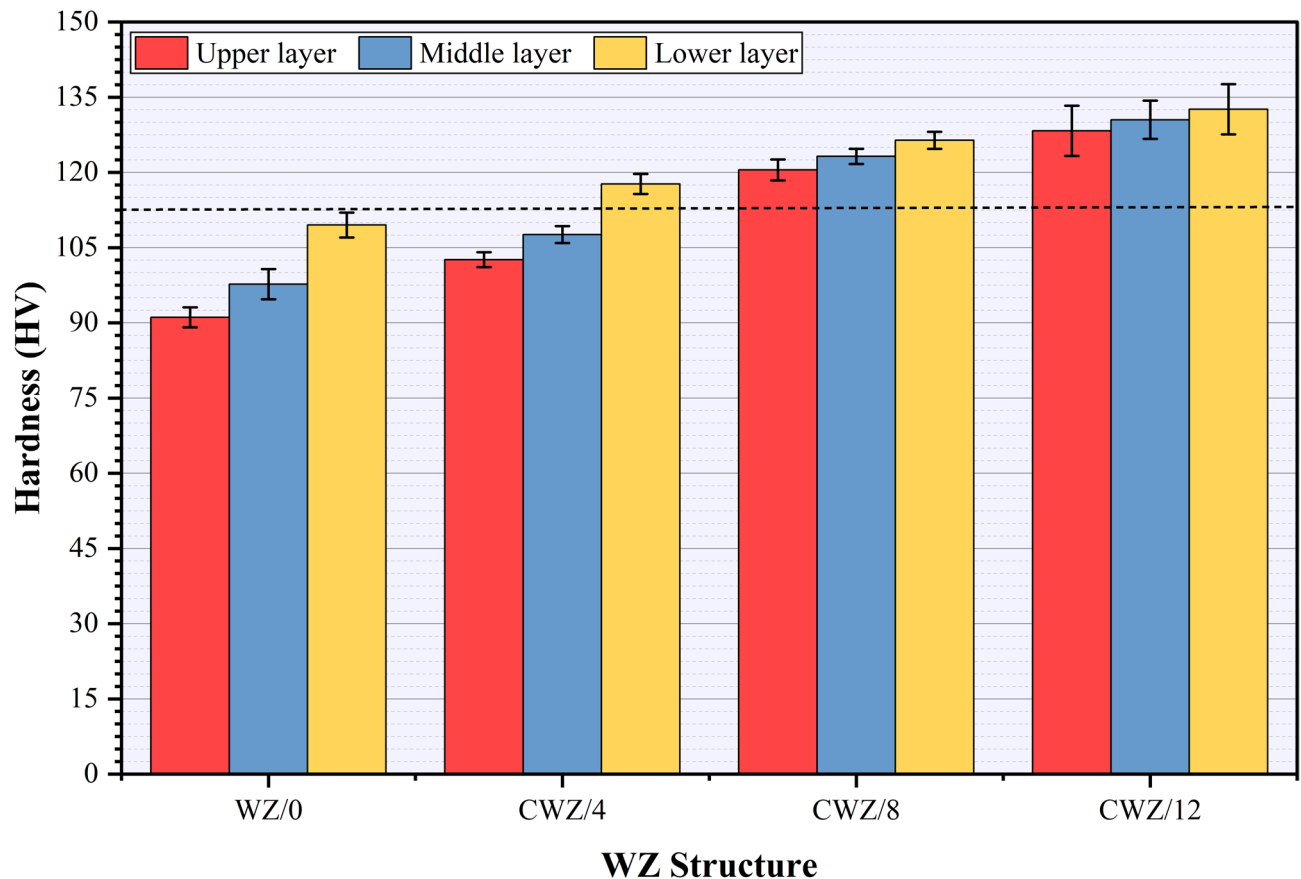


**Fig. 9.** WZ Vickers hardness measurements of WZ/0, CWZ/8, and CWZ/12 FSWed joints.

shown in Fig. 6. This increase in dislocation density indicates a higher degree of lattice distortion and strain fields around the  $\text{Al}_2\text{O}_3$  particles, which effectively impeded dislocation movement. The enhanced dislocation-particle interactions contributed significantly to the observed hardness improvement. Furthermore, the dislocation increment, which quantifies the strengthening contribution of dislocations, exhibited a similar upward trend. The dislocation increment increased from 29.65 MPa in the WZ/0 sample to 43.03 MPa in the CWZ/12 sample (Fig. 6). This substantial increase in the dislocation increment directly correlates with the hardness enhancement, as it represents the additional stress required for plastic deformation. In addition, microstrain analysis provides further evidence of the strengthening mechanisms. The microstrain increased from  $0.00167 \pm 1.07\text{E-}4$  in WZ/0 to  $0.00196 \pm 1.90\text{E-}4$  in CWZ/12, as illustrated in Fig. 6. This increase in microstrain indicates a higher level of lattice distortion and internal stress in the reinforced specimens, which is consistent with the presence of dispersed  $\text{Al}_2\text{O}_3$  particles and their interaction with the Al matrix. The combined effect of these mechanisms increased the dislocation density, dislocation increment, and microstrain, which explains the systematic enhancement in the hardness observed across all layers of the reinforced specimen. The progressive increase in hardness from CWZ/4 to CWZ/12 demonstrates the cumulative strengthening effect achieved by increasing the volume fraction of  $\text{Al}_2\text{O}_3$  particles. It can be concluded that the hardness enhancement ratios reveal a systematic improvement in the mechanical properties across different layers of the reinforced friction stir welded joints. Compared with the unreinforced WZ/0 specimen, the CWZ/12 joint exhibited enhancement ratios of 1.41, 1.34, and 1.21 for the upper, middle, and lower layers, respectively. The intermediate compositions showed progressive improvements, with CWZ/4 displaying enhancement ratios of 1.13, 1.10, and 1.07, whereas CWZ/8 demonstrated higher ratios of 1.32, 1.26, and 1.15 for the corresponding layers, as shown in Fig. 9.

### Corrosion analysis

The Potentiodynamic polarization results for the AA6082-T6 BM and the corresponding weld zones of the FSWed joints, including WZ/0, CWZ/4, CWZ/8, and CWZ/12, are presented in Table 3; Fig. 10. The  $i_{\text{corr}}$  values exhibited significant variations across different specimens. The AA6082-T6 BM exhibited a relatively low  $i_{\text{corr}}$  of  $2.34\text{E-}06 \text{ A/cm}^2$ , indicating good corrosion resistance. However, the unreinforced WZ/0 specimen displayed a notably higher  $i_{\text{corr}}$  of  $2.62\text{E-}05 \text{ A/cm}^2$  (Table 3), suggesting a decrease in corrosion resistance owing to the FSW. This increase can be attributed to microstructural changes and the dissolution of the strengthening precipitates during FSW. Previous studies have revealed that corrosion properties are strongly dependent on the applied FSW parameters<sup>66–68</sup>. Laska et al.<sup>69</sup> examined the corrosion properties of the AA6056 FSWed joints under 3.5 wt% NaCl solution and found that corrosion resistance varied substantially based on the processing parameters

Parameter	AA6082-T6	WZ	CWZ/4	CWZ/8	CWZ/12
Corrosion current $I_{\text{corr}}$ (A)	2.34E-05	2.62E-05	1.35E-05	2.84E-06	2.62E-06
Corrosion current density $i_{\text{corr}}$ (A/cm <sup>2</sup> )	2.34E-05	2.62E-05	1.35E-05	2.84E-06	2.62E-06
Corrosion potential $E_{\text{corr}}$ (V)	-1.406	-1.103	-0.558	-2.034	-1.452
Corrosion rate CR (mm/year)	0.0765	0.8566	0.4414	0.0929	0.0857

**Table 3.** Potentiodynamic polarization results of AA608-T6 BM and corresponding WZ of FSWed joints of WZ/0, CWZ/4, CWZ/8, and CWZ/12.

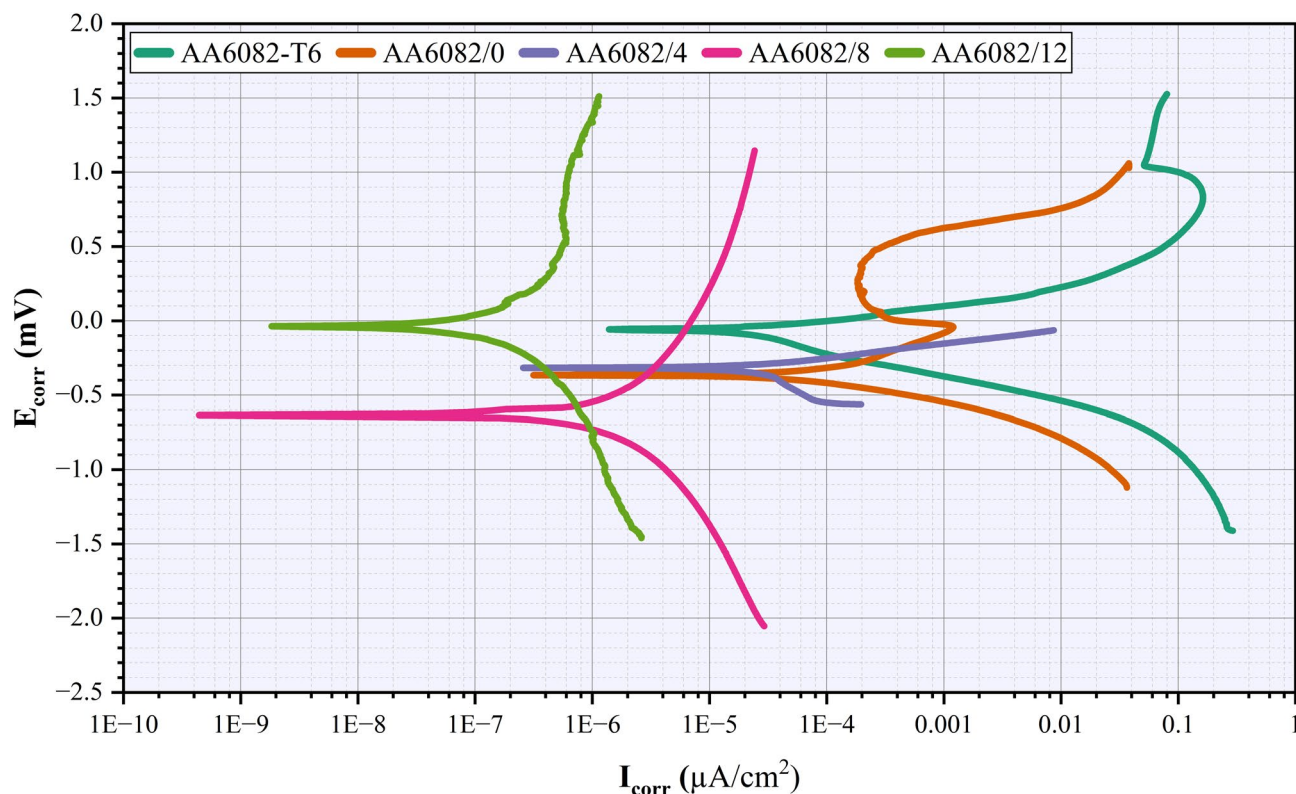


**Fig. 10.** Potentiodynamic polarization plots of the AA608-T6 BM and corresponding WZ of the FSWed joints of WZ/0, CWZ/4, CWZ/8, and CWZ/12.

employed. When higher welding speeds were used, the WZ pitting attack exhibited more diffuse characteristics with a reduced pit penetration depth. Conversely, joints produced at lower welding speeds displayed more concentrated and severe corrosion within the nugget zone than the AA6056 base material. Furthermore, an investigation by Padovani et al.<sup>68</sup> for the dissimilar FSW joints between AA2024 and AA7449 aluminum alloys revealed enhanced susceptibility to pitting corrosion, specifically within the welded region when exposed to 0.1 M NaCl solution. Interestingly, the incorporation of  $\text{Al}_2\text{O}_3$  particles led to a progressive improvement in corrosion resistance. The CWZ/4 specimen with 4 vol%  $\text{Al}_2\text{O}_3$ , shows a reduced  $i_{\text{corr}}$  of 1.35E-05 A/cm<sup>2</sup> compared to WZ/0. This trend continued with CWZ/8 and CWZ/12, which exhibited even lower  $i_{\text{corr}}$  values of 2.84E-06 A/cm<sup>2</sup> and 2.62E-06 A/cm<sup>2</sup>, respectively. These values are comparable to those of the BM, indicating that the addition of  $\text{Al}_2\text{O}_3$  particles effectively mitigated the corrosion susceptibility induced by the FSW process. In addition, the  $E_{\text{corr}}$  values provide further understanding of the electrochemical behavior of the specimens. The BM exhibited an  $E_{\text{corr}}$  of -1.406 V, whereas WZ/0 showed a slightly more noble potential of -1.103 V. The CWZ/4 specimen displayed the noblest  $E_{\text{corr}}$  at -0.558 V, suggesting a significant shift in its electrochemical behavior. However, CWZ/8 and CWZ/12 exhibited more negative  $E_{\text{corr}}$  values of -2.034 and -1.452 V, respectively. This non-linear trend in the  $E_{\text{corr}}$  values indicates complex interactions between the  $\text{Al}_2\text{O}_3$  particles and the aluminum matrix, potentially influencing the formation and stability of passive films. The CR data further corroborate the trends observed in the  $i_{\text{corr}}$  values. The BM exhibited a low CR of 0.0765 mm/year, which increased significantly to 0.8566 mm/year for the WZ/0. The addition of  $\text{Al}_2\text{O}_3$  particles led to a progressive decrease in CR, with

CWZ/12 showing a rate of 0.0857 mm/year, which is nearly equivalent to that of the BM (Table 3). This trend demonstrates the effectiveness of the  $\text{Al}_2\text{O}_3$  reinforcement in enhancing the corrosion resistance of FSW joints. In the same context, Fig. 10 illustrates the potentiodynamic polarization behaviors of the AA6082-T6 BM and corresponding weld zones. The polarization curves revealed distinct electrochemical characteristics, with the BM curve showing a stable passive region, indicative of superior corrosion resistance. The unreinforced WZ/0 curve demonstrates a higher current density and narrower passive region, corroborating the increased susceptibility to corrosion owing to microstructural instability. The reinforced zones, particularly CWZ/8 and CWZ/12, exhibited polarization curves with reduced current densities and extended passive regions, underscoring the role of  $\text{Al}_2\text{O}_3$  reinforcements in enhancing the corrosion resistance. These results demonstrate that the incorporation of  $\text{Al}_2\text{O}_3$  particles, particularly at higher concentrations, effectively counteracts the negative impact of FSW on the corrosion resistance of the AA6082-T6 joints. This improvement can be attributed to the modification of the microstructure, the creation of physical barriers to corrosion propagation, and potential changes in the passive film characteristics. The presence of  $\text{Al}_2\text{O}_3$  particles influenced the distribution and morphology of the intermetallic compounds, further contributing to the enhanced corrosion resistance. Previous studies have demonstrated that the  $\text{Al}_2\text{O}_3$  addition positively influences the corrosion resistance of Al-based composites by improving microstructural integrity and forming protective oxide layers<sup>70–72</sup>. In this context, Dwivedi and Sharma<sup>73</sup> highlighted the synergistic effects of clay and  $\text{Al}_2\text{O}_3$  reinforcements on the corrosion properties of Al-based composites. They concluded that the addition of  $\text{Al}_2\text{O}_3$  significantly improved the corrosion resistance by reducing the active surface area exposed to corrosive agents. Furthermore, W. Jiang et al.<sup>72</sup> investigated the impact of  $\text{Al}_2\text{O}_3$  in cold-sprayed coatings on the microstructure and corrosion behavior on the Al/ $\text{Al}_2\text{O}_3$  composite. The results showed that the  $\text{Al}_2\text{O}_3$ -enhanced coatings had superior microstructural integrity and corrosion resistance owing to the uniform distribution of  $\text{Al}_2\text{O}_3$  particles, which minimized galvanic corrosion and reinforced the Al matrix. In the current work, it can be remarked that the unreinforced WZ/0 joint exhibited an 11.2 times higher corrosion rate compared to the AA6082-T6 BM. However, the progressive addition of  $\text{Al}_2\text{O}_3$  nanoparticles remarkably improved the corrosion resistance. The corrosion rate decreased systematically with increasing  $\text{Al}_2\text{O}_3$  content, with CWZ/4 showing a 1.94 times reduction compared to WZ/0, and CWZ/8 achieving a 9.22 times reduction. The most significant improvement was observed for CWZ/12, which demonstrated a 10 times reduction in the corrosion rate compared with WZ/0. This enhancement brought the corrosion performance of CWZ/12 remarkably close to that of the base material, with only a 1.12 times higher corrosion rate, indicating that while FSW initially reduces the corrosion resistance of AA6082-T6 BM, the addition of  $\text{Al}_2\text{O}_3$  particles can effectively restore and even enhance the corrosion performance to levels comparable to or better than the BM, as shown in Table 3.

## Wear behavior and mechanisms

### Wear behavior

The wear behaviors of the AA6082-T6 BM and its corresponding FSWed joints, including those reinforced with  $\text{Al}_2\text{O}_3$  interlayers, were systematically evaluated under varying load conditions. Figure 11 presents the  $WV_i$  for the BM and WZ of the unreinforced (WZ/0) and reinforced (CWZ/4, CWZ/8, and CWZ/12) joints under applied loads of 5, 10, 20, and 30 N. The results of the  $WV_i$ , as shown in Fig. 11, reveal distinct trends in wear resistance across the different specimens. At the lowest applied load of 5 N, the AA6082-T6 BM exhibited a  $WV_i$  of  $20.41\text{E-}3 \text{ mm}^3$ . In comparison, the unreinforced WZ/0 joint exhibited a higher wear volumetric loss rate of  $24.41\text{E-}3 \text{ mm}^3/\text{m}$ , indicating reduced wear resistance in the weld zone. This difference in wear resistance can be directly attributed to the variations in hardness between the two regions. The lower hardness of the WZ/0 joint, owing to the dissolution of strengthening precipitates such as  $\text{Mg}_2\text{Si}$  during the FSW process, directly translates to reduced wear resistance, as evidenced by the higher  $WV_i$ . Softer materials are generally more susceptible to wear because they offer less resistance to plastic deformation and material removal during wear. The unreinforced WZ, with its lower hardness, is thus more prone to material loss under applied loads, resulting in the observed higher  $WV_i$  compared to the harder base metal. Interestingly, the incorporation of  $\text{Al}_2\text{O}_3$  particles led to a significant improvement in the wear resistance. The CWZ/4 joint, containing 4 vol%  $\text{Al}_2\text{O}_3$ , demonstrated a marked reduction in  $WV_i$  to  $11.31\text{E-}3 \text{ mm}^3/\text{m}$  under the 5 N load. This trend of enhanced wear resistance continued with increasing  $\text{Al}_2\text{O}_3$  content, with CWZ/8 and CWZ/12 exhibiting wear volume losses of  $10.93\text{E-}3 \text{ mm}^3/\text{m}$  and  $12.06 \text{ mm}^3/\text{m}$  (Fig. 11), respectively, at a 5 N load. As the applied load increased, a general trend of increasing  $WV_i$  was observed across all specimens. However, the relative performance of the reinforced joints compared to that of the BM and unreinforced WZ remained consistent. Under a 10 N load, for instance, the wear volume loss for the BM increased to  $29.81\text{E-}3 \text{ mm}^3$ , while the unreinforced WZ/0 showed a higher value of  $34.52\text{E-}3 \text{ mm}^3/\text{m}$ . The reinforced joints continued to demonstrate superior wear resistance, with CWZ/8 exhibiting the lowest wear volume loss of  $13.46\text{E-}3 \text{ mm}^3/\text{m}$  at this load, as depicted in Fig. 11. The wear behavior under higher loads of 20 N and 30 N followed similar patterns, with the reinforced joints consistently outperforming the BM and unreinforced WZ joints. However, it is noteworthy that at the highest load of 30 N, the wear resistance of CWZ/12 decreased significantly, with a  $WV_i$  of  $73.78\text{E-}3 \text{ mm}^3/\text{m}$ , approaching that of the unreinforced WZ/0 of  $78.26\text{E-}3 \text{ mm}^3/\text{m}$ , as shown in Fig. 11. This behavior of CWZ/12 is strongly correlated with the densification analysis; CWZ/12 exhibited the highest relative porosity of  $9.37 \pm 0.50\%$  (Fig. 8) among all the WZ of the FSWed joints. This high porosity disrupts the load-bearing capacity of the material and reduces its wear resistance under high loads. Porosity introduces stress concentration points and weakens the matrix-reinforcement interface, leading to accelerated material removal during wear testing. The enhanced wear resistance observed in the  $\text{Al}_2\text{O}_3$ -reinforced joints can be attributed to several factors. The presence of hard ceramic particles in the Al matrix acts as an obstacle to plastic deformation and material removal during the wear process. In addition, the increased dislocation density and strain hardening induced by the  $\text{Al}_2\text{O}_3$  particles, as evidenced by the XRD (Figs. 6 and 7) and hardness (Fig. 9) measurements, contributed to the



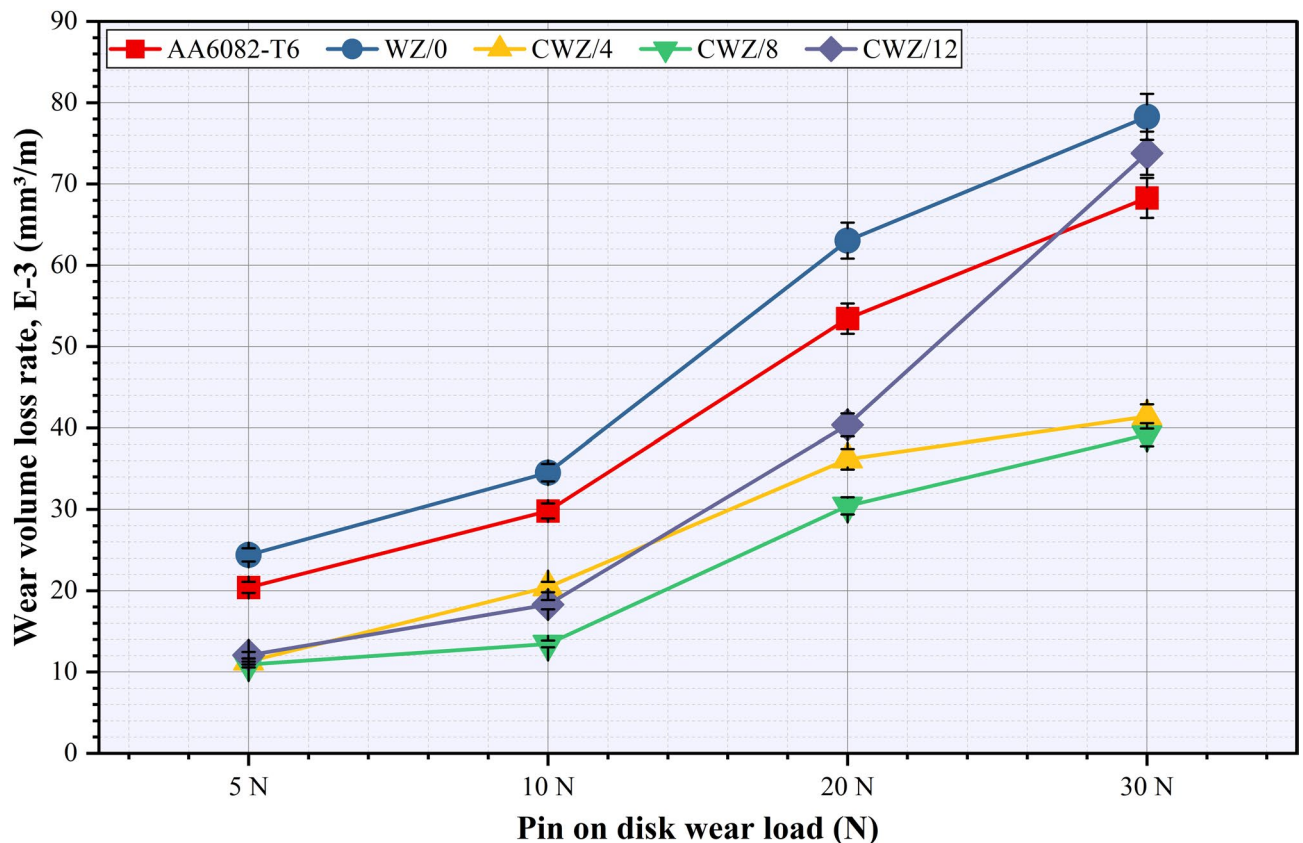


**Fig. 11.** Wear Behavior of the AA6082-T6 BM and corresponding WZ of FSWed joints of WZ/0, CWZ/4, CWZ/8, and CWZ/12.

overall improvement in wear resistance. It can be concluded that the wear behavior results revealed significant enhancement ratios for the  $\text{Al}_2\text{O}_3$ -reinforced FSWed joints compared to the unreinforced WZ/0 joint. Under a 5 N load, CWZ/4, CWZ/8, and CWZ/12 exhibited enhancement ratios of 2.16, 2.23, and 2.02, respectively. When the load was increased to 10 N, the enhancement ratios were 1.69, 2.56, and 1.89 for CWZ/4, CWZ/8, and CWZ/12, respectively. At 20 N, the ratios were 1.74, 2.07, and 1.56, whereas at the highest load of 30 N, they were 1.89, 2.00, and 1.06 for CWZ/4, CWZ/8, and CWZ/12, respectively. Notably, CWZ/8 consistently demonstrated the highest enhancement ratios under all load conditions, indicating optimal wear resistance.

#### Wear mechanisms

The wear mechanisms and surface features of the AA6082-T6 base BM and its corresponding FSWed joints were thoroughly examined using FE-SEM. Figure 12 shows FE-SEM micrographs of the worn surfaces at a higher wear load of 30 N for (a) AA6082-T6 and the corresponding WZ of the FSWed joints of (b) WZ/0, (c) CWZ/4, (d) CWZ/8, and (e) CWZ/12. The worn surface of the AA6082-T6 BM exhibited the characteristics of adhesive wear, as evidenced by the presence of adhesion marks and debris particles. The surface also exhibited shallow and wide grooves, indicative of abrasive wear mechanisms, as shown in Fig. 12a. This combination of adhesive and abrasive wear is typical for Al alloys under sliding conditions, where softer Al can adhere to the counterface and subsequently be sheared off, whereas harder asperities or wear debris can plow through the surface. The unreinforced WZ/0 specimen exhibited more severe wear features than the BM. The SEM micrographs revealed extensive adhesion, severe flake-like debris, and the formation of microcracks. In addition, delamination was observed, suggesting a fatigue-based wear mechanism (Fig. 12b). With the incorporation of the  $\text{Al}_2\text{O}_3$  reinforcement, a notable transition in the wear mechanism was observed. The CWZ/4 specimen, containing 4 vol%  $\text{Al}_2\text{O}_3$ , exhibited shallow and wide grooves along with micro-grooves. Interestingly, some grooves appeared incomplete (Fig. 12c), suggesting that the ceramic particles interrupted the continuity of the abrasive wear tracks. As the  $\text{Al}_2\text{O}_3$  content increased to 8 vol% in the CWZ/8 specimen, the wear features transitioned to micro narrow and shallow grooves (Fig. 12d). Evidence of plastic deformation was also observed, likely due to the interaction between the harder ceramic particles and softer Al matrix. The presence of ceramic particles on the worn surface was more pronounced, suggesting their effectiveness in bearing the applied load and resisting the wear. The CWZ/12 specimen, which had the highest  $\text{Al}_2\text{O}_3$  content of 12 vol%, displayed shallow and narrow grooves along with signs of plastic deformation (Fig. 12e). Ceramic particles were visible on the worn surface, indicating their significant role in modifying wear behavior. The narrower grooves compared with those in CWZ/4 and CWZ/8 suggest a further reduction in the severity of abrasive wear. These observations

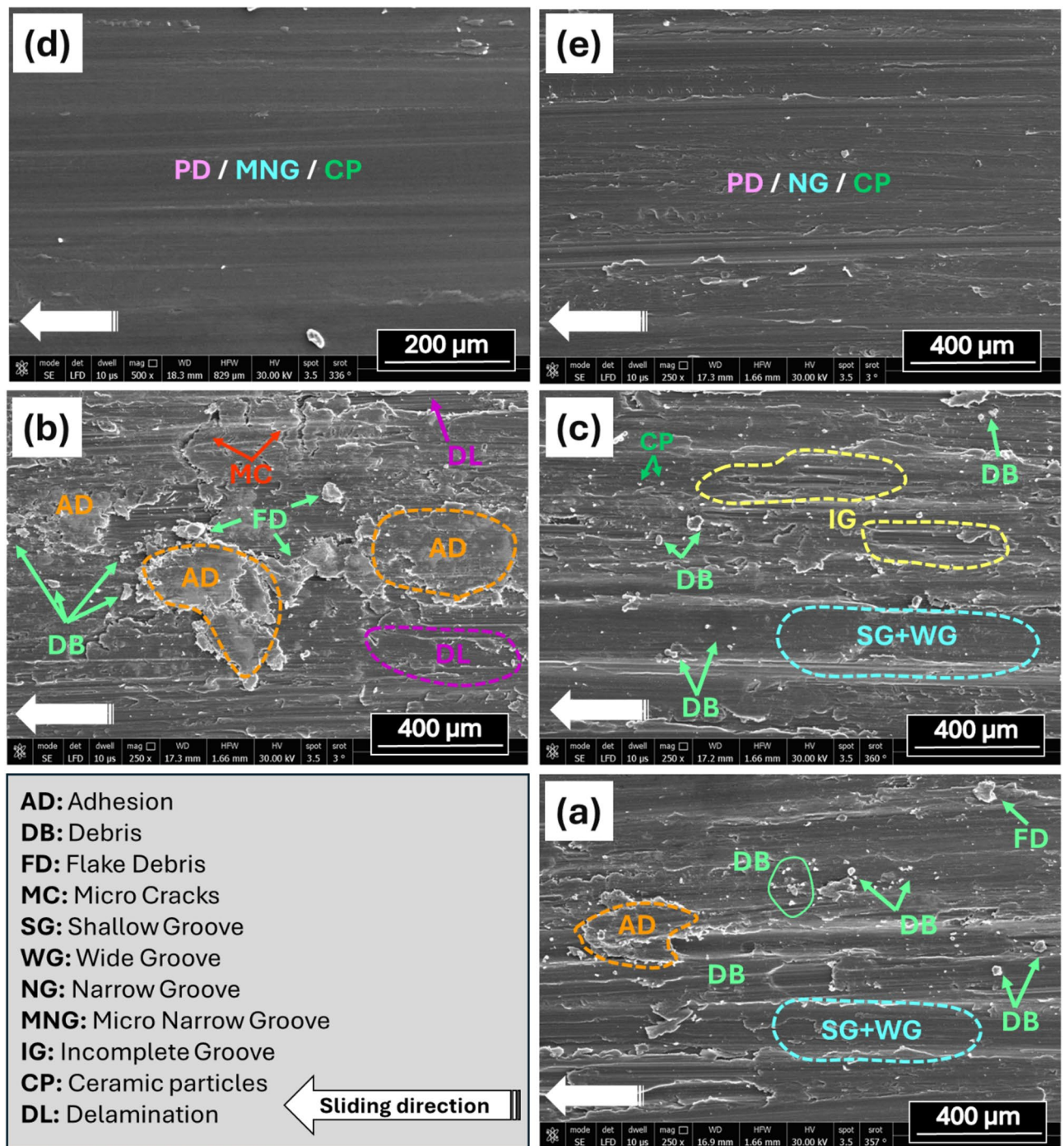


**Fig. 12.** Wear features of worn surfaces for WZ wear-tested specimens of (a) AA6082-T6 and the corresponding WZ of the FSWed joints of (b) WZ/0, (c) CWZ/4, (d) CWZ/8, and (e) CWZ/12, at a higher wear load of 30 N.

collectively demonstrate a progressive transition in the wear mechanisms with an increase in the  $\text{Al}_2\text{O}_3$  content. The unreinforced WZ/0 exhibited severe adhesive and fatigue-based wear, whereas the introduction of  $\text{Al}_2\text{O}_3$  particles led to a shift towards milder abrasive wear with an increasing resistance to plastic deformation. This transition can be attributed to several factors: the hard  $\text{Al}_2\text{O}_3$  particles acted as load-bearing elements, reducing direct metal-to-metal contact and mitigating adhesive wear. Furthermore, the ceramic particles provided localized reinforcement, enhancing the overall hardness and wear resistance of CWZ. In addition, as the  $\text{Al}_2\text{O}_3$  content increased, the particles formed a more effective barrier against abrasive wear, resulting in narrower and shallower wear grooves. However, it is important to note that while a higher  $\text{Al}_2\text{O}_3$  content generally improves wear resistance, excessive reinforcement, as in the CWZ/12 joints, may lead to particle clustering and potential

stress concentration points. This could explain the slight increase in the wear volume loss observed for CWZ/12 under higher loads, as discussed earlier (Fig. 11; wear behavior section).

## Conclusion

This study investigated the microstructural, tribological, and corrosion behaviors of AA6082-T6 friction stir welded joints reinforced with  $\text{Al}_2\text{O}_3$  interlayer strips. The key findings and their implications are as follows:

- The incorporation of  $\text{Al}_2\text{O}_3$  particles led to significant grain refinement in the CWZ. The crystallite size decreased from 154.89 nm in the unreinforced weld zone of WZ/0 to 106.73 nm in the CWZ/12 zone, indicating a 31% reduction in the crystallite size. This refinement was accompanied by an increase in the dislocation density from  $4.16\text{E-}5\text{ nm}^{-2}$  to  $8.77\text{E-}5\text{ nm}^{-2}$ , representing a 111% increase.
- The hardness of the WZ systematically improved with increasing  $\text{Al}_2\text{O}_3$  content. The CWZ/12 specimen exhibited hardness values of 128.3 HV, 130.5 HV, and 132.6 HV across the upper, middle, and lower layers, respectively, compared to 91.1 HV, 97.6 HV, and 109.5 HV in the unreinforced WZ/0 specimen. This represents a significant enhancement of up to 41% in hardness, demonstrating the effectiveness of the  $\text{Al}_2\text{O}_3$  reinforcement in mitigating the typical softening observed in FSWed joints.
- The corrosion resistance of the WZ was significantly improved with the  $\text{Al}_2\text{O}_3$  reinforcement. The corrosion rate decreased from 0.8566 mm/y in WZ/0 to 0.0857 mm/y in CWZ/12, approaching the AA6082-T6 BM corrosion rate of 0.0765 mm/y. This 90% reduction in CR highlights the potential of  $\text{Al}_2\text{O}_3$  reinforcement to enhance the durability of FSWed joints in corrosive environments.
- The wear behavior of the reinforced joints showed significant improvement under various load conditions. Under a 10 N load, the  $WV_i$  decreased from  $34.52\text{E-}3\text{ mm}^3/\text{m}$  in WZ/0 to  $13.46\text{E-}3\text{ mm}^3/\text{m}$  in CWZ/8, representing a 61% reduction. The wear mechanism transitioned from severe adhesive and fatigue-based wear in the WZ/0 to milder abrasive wear in the reinforced joints, indicating enhanced surface durability.
- While increasing the  $\text{Al}_2\text{O}_3$  content generally improved the properties, this study identified an optimal reinforcement level. The CWZ/8 specimen, containing 8 vol%  $\text{Al}_2\text{O}_3$ , consistently demonstrated the best overall performance in terms of wear resistance and balanced improvement in other properties.

This study demonstrates that the strategic incorporation of an  $\text{Al}_2\text{O}_3$  interlayer reinforcement can effectively counteract the typical softening and property degradation observed in FSWed joints of AA6082-T6 alloys. Future research should focus on the following aspects:

- The FSW parameters were optimized in conjunction with  $\text{Al}_2\text{O}_3$  reinforcement to further enhance the joint properties.
- Exploration of hybrid reinforcement strategies combining  $\text{Al}_2\text{O}_3$  with other ceramic or metallic particles to achieve synergistic property enhancement.

## Data availability

The datasets used and/or analysed during the current study available from the corresponding author on reasonable request.

Received: 11 February 2025; Accepted: 23 May 2025

Published online: 01 July 2025

## References

1. Miller, W. S. et al. Recent development in aluminium alloys for the automotive industry. *Mater. Sci. Engineering: A*. **280**, 37–49. [https://doi.org/10.1016/S0921-5093\(99\)00653-X](https://doi.org/10.1016/S0921-5093(99)00653-X) (2000).
2. Noga, P., Skrzekut, T., Wędrychowicz, M., Węglowski, M. S. & Węglowska, A. Research of friction stir welding (FSW) and Electron beam welding (EBW) process for 6082-T6 aluminum alloy. *Materials* **16**, 4937. <https://doi.org/10.3390/ma16144937> (2023).
3. Noga, P., Piotrowicz, A., Skrzekut, T., Zwoliński, A. & Strzępek, P. Effect of various forms of aluminum 6082 on the mechanical properties, microstructure and surface modification of the profile after extrusion process. *Materials* **14**, 5066. <https://doi.org/10.3390/ma14175066> (2021).
4. Habba, M. I. A. et al. Comparative Study of FSW, MIG, and TIG Welding of AA5083-H111 Based on the Evaluation of Welded Joints and Economic Aspect. *Materials* **16**. (2023).
5. Ahmed, M. M. Z., El-Sayed Seleman, M. M., Fydyrych, D. & Çam, G. Review on friction stir welding of dissimilar magnesium and aluminum alloys: scientometric analysis and strategies for achieving High-Quality joints. *J. Magnesium Alloys*. **Accepted** <https://doi.org/10.1016/j.jma.2023.09.039> (2023).
6. Habba, M. I. A. & Ahmed, M. M. Z. Friction stir welding of dissimilar aluminum and copper alloys: A review of strategies for enhancing joint quality. *J. Adv. Join. Processes*. **11**, 100293. <https://doi.org/10.1016/J.JAJP.2025.100293> (2025).
7. Albaijan, I. et al. Optimization of Bobbin Tool Friction Stir Processing Parameters of AA1050 Using Response Surface Methodology. *Materials* (2022).
8. Saha, R. & Biswas, P. Current status and development of external Energy-Assisted friction stir welding processes: A review. *Weld. World*. **66**, 577–609. <https://doi.org/10.1007/s40194-021-01228-7> (2022).
9. Ahmed, M. M. Z. et al. Microstructure and mechanical properties of dissimilar friction stir welded AA2024-T4/AA7075-T6 T-Butt joints. *Met. (Basel)*. **11**, 1–19. <https://doi.org/10.3390/met11010128> (2021).
10. Sahu, P. K. & Pal, S. Mechanical properties of dissimilar thickness aluminium alloy weld by single/double pass FSW. *J. Mater. Process. Technol.* **243**, 442–455. <https://doi.org/10.1016/j.jmatprotec.2017.01.009> (2017).
11. Cabibbo, M., Forcellese, A., El Mehtedi, M. & Simoncini, M. Double side friction stir welding of AA6082 sheets: microstructure and nanoindentation characterization. *Mater. Sci. Engineering: A*. **590**, 209–217. <https://doi.org/10.1016/j.msea.2013.10.031> (2014).
12. Ahmed, M. M. Z., Touileb, K., El-Sayed Seleman, M. M., Albaijan, I. & Habba, M. I. A. Bobbin tool friction stir welding of aluminum: parameters optimization using Taguchi experimental design. *Materials* **15** <https://doi.org/10.3390/ma15082771> (2022).



13. Malopheyev, S., Vysotskiy, I., Kulitskiy, V., Mironov, S. & Kaibyshev, R. Optimization of Processing-Microstructure-Properties relationship in Friction-Stir welded 6061-T6 aluminum alloy. *Mater. Sci. Engineering: A*. **662**, 136–143. <https://doi.org/10.1016/j.msea.2016.03.063> (2016).
14. Al-Sabur, R. Tensile strength prediction of aluminium alloys welded by FSW using response surface Methodology – Comparative review. *Mater. Today Proc.* **45**, 4504–4510. <https://doi.org/10.1016/j.matpr.2020.12.1001> (2021).
15. Wahid, M. A., Siddiquee, A. N., Khan, Z. A. & Sharma, N. Analysis of cooling media effects on microstructure and mechanical properties during FSW/UFSW of AA 6082-T6. *Mater. Res. Express*. **5**, 046512. <https://doi.org/10.1088/2053-1591/aab8e3> (2018).
16. Salih, O. S., Ou, H., Sun, W. H. & Generation Plastic deformation and residual stresses in friction stir welding of aluminium alloy. *Int. J. Mech. Sci.* **238**, 107827. <https://doi.org/10.1016/j.ijmecsci.2022.107827> (2023).
17. Essa, A. R. S. et al. Friction stir welding of aluminum alloy 6082-T6 using eccentric shoulder tools to eliminate the need for tool tilting. *Sci. Rep.* **15**, 8801. <https://doi.org/10.1038/s41598-025-91065-1> (2025).
18. Hamada, A. S. et al. The microstructural evolution of friction stir welded AA6082-T6 aluminum alloy during Cyclic deformation. *Mater. Sci. Engineering: A*. **642**, 366–376. <https://doi.org/10.1016/j.msea.2015.06.100> (2015).
19. Tamadon, A., Pons, D. J., Sued, K. & Clucas, D. Thermomechanical grain refinement in AA6082-T6 thin plates under bobbin friction stir welding. *Met. (Basel)*. **8**, 375. <https://doi.org/10.3390/met8060375> (2018).
20. Aleem Pasha, M., Ravinder Reddy, P., Laxminarayana, P. & Khan, I. A. SiC and Al<sub>2</sub>O<sub>3</sub> Reinforced Friction Stir Welded Joint of Aluminium Alloy 6061. In *Springer Nature*; Springer, Singapore, ; pp. 163–182 ISBN 978-981-13-0377-7. (2019).
21. Guo, J., Gougeon, P. & Chen, X. G. Microstructure evolution and mechanical properties of dissimilar friction stir welded joints between AA1100-B 4 C MMC and AA6063 alloy. *Mater. Sci. Eng., A*. **553**, 149–156. <https://doi.org/10.1016/j.msea.2012.06.004> (2012).
22. Mirjavadi, S. S. et al. Influence of TiO<sub>2</sub> nanoparticles incorporation to friction stir welded 5083 aluminum alloy on the microstructure, mechanical properties and wear resistance. *J. Alloys Compd.* **712**, 795–803. <https://doi.org/10.1016/j.jallcom.2017.04.114> (2017).
23. Li, C., Feng, X., Shen, Y. & Chen, W. Preparation of Al<sub>2</sub>O<sub>3</sub>/TiO<sub>2</sub> Particle-Reinforced copper through plasma spraying and friction stir processing. *Mater. Des.* **90**, 922–930. <https://doi.org/10.1016/j.matdes.2015.11.047> (2016).
24. Habba, M. I. A., Barakat, W. S., Elnekhaily, S. A. & Hamid, F. S. Microstructure and tribological behavior of Al–TiC composite strips fabricated by a Multi-Step densification method. *Sci. Rep.* **14**, 1–21. <https://doi.org/10.1038/s41598-024-70560-x> (2024).
25. Refat, M., Abdelmotagaly, A. M. M., Ahmed, M. M. Z. & El-Mahallawi, I. The effect of heat treatment on the properties of friction stir processed AA7075-O with and without nano alumina additions. *Friction Stir Weld. Process. VIII*. 115–123. [https://doi.org/10.1007/978-3-319-48173-9\\_13](https://doi.org/10.1007/978-3-319-48173-9_13) (2016).
26. Ahmed, M. M. Z., Refat, M. & El-Mahallawi, I. Manufacturing of Nano-Surface AA7075 composites by friction stir processing. *Light Met.* **2014**. **9781118889**, 1417–1422. <https://doi.org/10.1002/9781118888438.ch237> (2014).
27. Bhavya Swathi, I., Suvarna Raju, L. & Ramulu, P. J. Surface development by reinforcing Nano-Composites during friction stir Processing – a review. *J. Eng. Des. Technol.* **18**, 653–687. <https://doi.org/10.1108/JEDT-02-2019-0043> (2020).
28. Farahmand Nikoo, M., Azizi, H., Parvin, N. & Yousefpour Naghibi, H. The influence of heat treatment on microstructure and wear properties of friction stir welded AA6061-T6/Al<sub>2</sub>O<sub>3</sub> nanocomposite joint at four different traveling speed. *J. Manuf. Process.* **22**, 90–98. <https://doi.org/10.1016/j.jmapro.2016.01.003> (2016).
29. Srivastava, M. & Rathee, S. A. Study on the effect of incorporation of SiC particles during friction stir welding of al 5059 alloy. *Silicon* **13**, 2209–2219. <https://doi.org/10.1007/s12633-020-00722-9> (2021).
30. Abu-Okail, M., Abu-Oqail, A. & Ata, M. H. Effect of friction stir welding process parameters with interlayer strip on microstructural characterization and mechanical properties. *J. Fail. Anal. Prev.* **20**, 173–183. <https://doi.org/10.1007/s11668-020-00813-0> (2020).
31. Sadoun, A. M., Meselhy, A. F. & Deabs, A. W. Improved strength and ductility of friction stir Tailor-Welded blanks of base metal AA2024 reinforced with interlayer strip of AA7075. *Results Phys.* **16**, 102911. <https://doi.org/10.1016/j.rinp.2019.102911> (2020).
32. Zheng, B. et al. Effect of Sn interlayer on mechanical properties and microstructure in al/mg friction stir lap welding with different rotational speeds. *Mater. Res. Express*. **7** <https://doi.org/10.1088/2053-1591/ab9fbb> (2020).
33. Sahu, P. K., Pal, S. & Pal, S. K. Al/Cu dissimilar friction stir welding with ni, ti, and Zn foil as the interlayer for flow control, enhancing mechanical and metallurgical properties. *Metall. Mater. Trans. Phys. Metall. Mater. Sci.* **48**, 3300–3317. <https://doi.org/10.1007/s11661-017-4093-y> (2017).
34. Maity, D. & Racherla, V. Effect of SiC interlayer on microstructure and joint strength of Cu-Al welds obtained using a new friction processing method. *CIRP J. Manuf. Sci. Technol.* **52**, 73–85. <https://doi.org/10.1016/j.cirpj.2024.05.009> (2024).
35. Hou, W. et al. Enhancing metallurgical and mechanical properties of friction stir butt welded joints of Al–Cu via cold sprayed Ni interlayer. *Mater. Sci. Engineering: A*. **809** <https://doi.org/10.1016/j.msea.2021.140992> (2021).
36. Khojastehnezhad, V. M. & Pourasl, H. H. Microstructural characterization and mechanical properties of aluminum 6061-T6 plates welded with copper insert plate (Al/Cu/Al) using friction stir welding. *Trans. Nonferrous Met. Soc. China*. **28**, 415–426. [https://doi.org/10.1016/S1003-6326\(18\)64675-8](https://doi.org/10.1016/S1003-6326(18)64675-8) (2018).
37. Anand, R. & Sridhar, V. G. Effects of SiC and Al<sub>2</sub>O<sub>3</sub> reinforcement of varied volume fractions on mechanical and Micro structure properties of interlock FSW dissimilar joints AA7075-T6-AA7475-T7. *Silicon* **13**, 3017–3029. <https://doi.org/10.1007/s12633-020-00630-y> (2021).
38. Ahmed, M. M. Z. et al. Heat input and mechanical properties investigation of friction stir welded Aa5083/Aa5754 and Aa5083/Aa7020. *Met. (Basel)*. **11**, 1–20. <https://doi.org/10.3390/met11010068> (2021).
39. Ataya, S. et al. Effective range of FSSW parameters for high Load-Carrying capacity of dissimilar steel A283M-C/Brass CuZn40 joints. *Materials* **15**, 1–25. <https://doi.org/10.3390/ma15041394> (2022).
40. Ahmed, M. M. Z. et al. Microstructure and Mechanical Properties of Friction Stir Welded 2205 Duplex Stainless Steel Butt Joints. *Materials* **14**. (2021).
41. Alsaleh, N. A. et al. Additively manufactured parts from AA2011-T6 Large-Diameter feedstocks using friction stir deposition. *Materials* **16**, 1–21. <https://doi.org/10.3390/ma16144904> (2023).
42. Essa, A. R. S. et al. Modeling and experimental investigation of the impact of the hemispherical tool on heat generation and tensile properties of dissimilar friction stir welded AA5083 and AA7075 al alloys. *Materials* **17** <https://doi.org/10.3390/ma17020433> (2024).
43. Guo, N., Fu, Y., Wang, Y., Meng, Q. & Zhu, Y. Microstructure and mechanical properties in friction stir welded 5A06 aluminum alloy Thick plate. *Mater. Des.* **113**, 273–283. <https://doi.org/10.1016/j.matdes.2016.10.030> (2017).
44. Cavaliere, P., Cerri, E., Marzoli, L. & Dos Santos, J. Friction stir welding of ceramic particle reinforced aluminium based metal matrix composites. *Appl. Compos. Mater.* **11**, 247–258. <https://doi.org/10.1023/B:ACMA.0000035478.71092.ec> (2004).
45. Jain, S. & Mishra, R. S. Effect of al 2 O 3 nanoparticles on microstructure and mechanical properties of friction Stir-Welded dissimilar aluminum alloys AA7075-T6 and AA6061-T6. *Proc. Institution Mech. Eng. Part. E: J. Process. Mech. Eng.* **236**, 1511–1521. <https://doi.org/10.1177/09544089211065534> (2022).
46. Haolin, D., Cui, W., Yunlong, H., Xin, C. & Yubo, D. Preparation of thermally conductive polyimide/aluminum oxide/boehmite composite separators for enhancing Lithium-ion battery safety and performance. *J. Appl. Polym. Sci.* **141** <https://doi.org/10.1002/app.56049> (2024).
47. Wei, H. et al. Aluminum-Based ceramic/metal composites with tailored thermal expansion fabricated by spark plasma sintering. *RSC Adv.* **14**, 3952–3961. <https://doi.org/10.1039/D3RA07593A> (2024).

48. Wang, C. et al. Facile fabrication of densely packed ammoniated alumina/mxene/bacterial cellulose composite films for enhancing thermal conductivity and photothermal conversion performance. *J. Mater. Sci. Technol.* **213**, 162–173. <https://doi.org/10.1016/j.jmst.2024.06.024> (2025).
49. Barakat, W. S., Habba, M. I. A., Ibrahim, A., Fathy, A. & Elkady, O. A. The effect of Cu coated  $\text{Al}_2\text{O}_3$  particle content and densification methods on the microstructure and mechanical properties of Al matrix composites. *J. Mater. Res. Technol.* **24**, 6908–6922. <https://doi.org/10.1016/j.jmrt.2023.05.010> (2023).
50. Ahmed, M. S. I. et al. Cladding of carbon steel with stainless steel using friction stir welding: effect of process parameters on microstructure and mechanical properties. *Cryst. (Basel)*. **13**, 1559. <https://doi.org/10.3390/cryst13111559> (2023).
51. El-Fahhar, H. H. et al. Effect of Post-Weld Heat-Treatment and Solid-State thermomechanical treatment on the properties of the AA6082 MIG welded joints. *Sci. Rep.* **14** <https://doi.org/10.1038/s41598-024-53795-6> (2024).
52. Aziz, S. B. et al. Impact of friction stir welding (FSW) process parameters on thermal modeling and heat generation of aluminum alloy joints. *Acta Metall. Sinica (English Letters)*. **29**, 869–883. <https://doi.org/10.1007/s40195-016-0466-2> (2016).
53. Durdanović, M. B., Mijajlović, M. M., Milčić, D. S. & Stamenković, D. S. Heat generation during friction stir welding process. *Tribology Ind.* **31**, 8–14 (2009).
54. Williamson, G. K. & Smallman, R. E. III Dislocation densities in some annealed and Cold-Worked metals from measurements on the X-Ray Debye-Scherrer spectrum. *Phil. Mag.* **1**, 34–46. <https://doi.org/10.1080/14786435608238074> (1956).
55. Williamson, G. K. & Hall, W. H. X-Ray line broadening from filed aluminium and Wolfram. *Acta Metall.* **1**, 22–31. [https://doi.org/10.1016/0001-6160\(53\)90006-6](https://doi.org/10.1016/0001-6160(53)90006-6) (1953).
56. Gu, C., Yang, X., Tang, W., Luo, T. & Wang, R. Softening behavior of stationary shoulder friction stir welded joint for Thick-Plate Al–Li–Cu alloy. *J. Mater. Res. Technol.* **20**, 3008–3024. <https://doi.org/10.1016/j.jmrt.2022.08.060> (2022).
57. Hansen, N. Boundary strengthening over five length scales. *Adv. Eng. Mater.* **7**, 815–821. <https://doi.org/10.1002/adem.200500102> (2005).
58. Ahmed, M. M. Z., Seleman, M. M. E., Eid, R. G. & Zawrah, M. F. Production of AA1050/Silica fume composite by bobbin Tool-Friction stir processing\_ microstructure, composition and mechanical properties. *CIRP J. Manuf. Sci. Technol.* **38**, 801–812. <https://doi.org/10.1016/j.cirpj.2022.07.002> (2022).
59. Akbari, M. K., Baharvandi, H. & Mirzaee, O. Investigation of particle size and reinforcement content on mechanical properties and fracture behavior of A356–Al<sub>2</sub>O<sub>3</sub> composite fabricated by Vortex method. *J. Compos. Mater.* **48**, 3315–3330. <https://doi.org/10.1177/0021998313507618> (2014).
60. Mazahery, A. & Ostadshabani, M. Investigation on mechanical properties of Nano-Al<sub>2</sub>O<sub>3</sub>-Reinforced aluminum matrix composites. *J. Compos. Mater.* **45**, 2579–2586. <https://doi.org/10.1177/0021998311401111> (2011).
61. Rahimian, M., Ehsani, N., Parvin, N. & Baharvandi, H. R. The effect of sintering temperature and the amount of reinforcement on the properties of Al–Al<sub>2</sub>O<sub>3</sub> composite. *Mater. Des.* **30**, 3333–3337. <https://doi.org/10.1016/j.matdes.2008.11.027> (2009).
62. Razavi-Tousi, S. S., Yazdani-Rad, R. & Manafi, S. A. Effect of volume fraction and particle size of alumina reinforcement on compaction and densification behavior of Al–Al<sub>2</sub>O<sub>3</sub> nanocomposites. *Mater. Sci. Engineering: A*. **528**, 1105–1110. <https://doi.org/10.1016/j.msea.2010.09.085> (2011).
63. Gong, W. B., Zhu, R., Qie, X. Z., Cui, H. & Gong, M. Y. Microstructure and Properties of 6082 Aluminum Alloy Ultra-Thick Plate Prepared by Friction Stir Weld. *Jilin Daxue Xuebao (Gongxueban)/Journal of Jilin University (Engineering and Technology Edition)* **50**, 512–519, (2020). <https://doi.org/10.13229/j.cnki.jdxbgxb20190241>
64. Perrett, J. G., Martin, J., Threadgill, P. L. & Ahmed, M. M. Z. Recent Developments in Friction Stir Welding of Thick Section Aluminium Alloys. (2007).
65. Rao, T. S., Reddy, G. M. & Rao, S. R. K. Microstructure and mechanical properties of friction stir welded AA7075–T651 aluminum alloy Thick plates. *Trans. Nonferrous Met. Soc. China (English Edition)*. **25**, 1770–1778. [https://doi.org/10.1016/S1006-6326\(15\)63782-7](https://doi.org/10.1016/S1006-6326(15)63782-7) (2015).
66. Jariyaboon, M. et al. The effect of welding parameters on the corrosion behaviour of friction stir welded AA2024–T351. *Corros. Sci.* **49**, 877–909. <https://doi.org/10.1016/j.corsci.2006.05.038> (2007).
67. Monetta, T., Montuori, M., Squillace, A. & Bellucci, F. The effect of heat treatment and welding parameters on the corrosion behaviour of a friction stir welded 6056 aluminium alloy. *Adv. Mat. Res.* **38**, 285–297. <https://doi.org/10.4028/www.scientific.net/AMR.38.285> (2008).
68. Padovani, C. G. et al. CORROSION AND PROTECTION OF FRICTION STIR WELDS IN AEROSPACE ALUMINIUM ALLOYS.
69. Laska, A., Szkodo, M., Koszelow, D. & Cavaliere, P. Effect of processing parameters on strength and corrosion resistance of friction Stir-Welded AA6082. *Met. (Basel)*. **12**, 192. <https://doi.org/10.3390/met12020192> (2022).
70. Huo, H. & Tjong, S. C. Corrosion behavior of Al-based composites containing *In-situ* TiB<sub>2</sub>, Al<sub>2</sub>O<sub>3</sub> and Al<sub>3</sub>Ti reinforcements in aerated 3.5% sodium chloride solution. *Adv. Eng. Mater.* **9**, 588–593. <https://doi.org/10.1002/adem.200700001> (2007).
71. Çalgılı, U., Kaçmı, M. V., Karabacak, A. H., Çanakçı, A. & Özkaya, S. Investigation of corrosion resistance and impact performance properties of Al<sub>2</sub>O<sub>3</sub>/SiC-Doped Aluminium-Based composites. *Bull. Mater. Sci.* **46**, 156. <https://doi.org/10.1007/s12034-023-02998-0> (2023).
72. Jiang, W. et al. Effect of Al<sub>2</sub>O<sub>3</sub> on microstructure and corrosion characteristics of Al/Al<sub>2</sub>O<sub>3</sub> composite coatings prepared by cold spraying. *Met. (Basel)*. **14** <https://doi.org/10.3390/met14020179> (2024).
73. Dwivedi, S. P. & Sharma, S. Tribological, corrosion, mechanical, and metallurgical behavior of clay and Al<sub>2</sub>O<sub>3</sub>-Reinforced aluminum-Based composite material. *Proc. Institution Mech. Eng. Part. E: J. Process. Mech. Eng.* <https://doi.org/10.1177/09544089241234433> (2024).

## Acknowledgements

The authors extend their appreciation to Prince Sattam bin Abdulaziz University for funding this research work through the project number (PSAU/2024/01/28387).

## Author contributions

A.O.: Methodology, Investigation, Writing – review & editing. M. I. A. H.: Conceptualization, Formal analysis, Investigation, Writing – original draft, Writing – review & editing. M. M. Z. A.: Conceptualization, Project Supervision, Funding, Writing – review & editing. W. S. B.: Conceptualization, Methodology, Investigation, Validation, Writing – original draft.

## Declarations

## Competing interests

The authors declare no competing interests.

### Additional information

**Correspondence** and requests for materials should be addressed to M.M.Z.A.

**Reprints and permissions information** is available at [www.nature.com/reprints](http://www.nature.com/reprints).

**Publisher's note** Springer Nature remains neutral with regard to jurisdictional claims in published maps and institutional affiliations.

**Open Access** This article is licensed under a Creative Commons Attribution-NonCommercial-NoDerivatives 4.0 International License, which permits any non-commercial use, sharing, distribution and reproduction in any medium or format, as long as you give appropriate credit to the original author(s) and the source, provide a link to the Creative Commons licence, and indicate if you modified the licensed material. You do not have permission under this licence to share adapted material derived from this article or parts of it. The images or other third party material in this article are included in the article's Creative Commons licence, unless indicated otherwise in a credit line to the material. If material is not included in the article's Creative Commons licence and your intended use is not permitted by statutory regulation or exceeds the permitted use, you will need to obtain permission directly from the copyright holder. To view a copy of this licence, visit <http://creativecommons.org/licenses/by-nc-nd/4.0/>.

© The Author(s) 2025